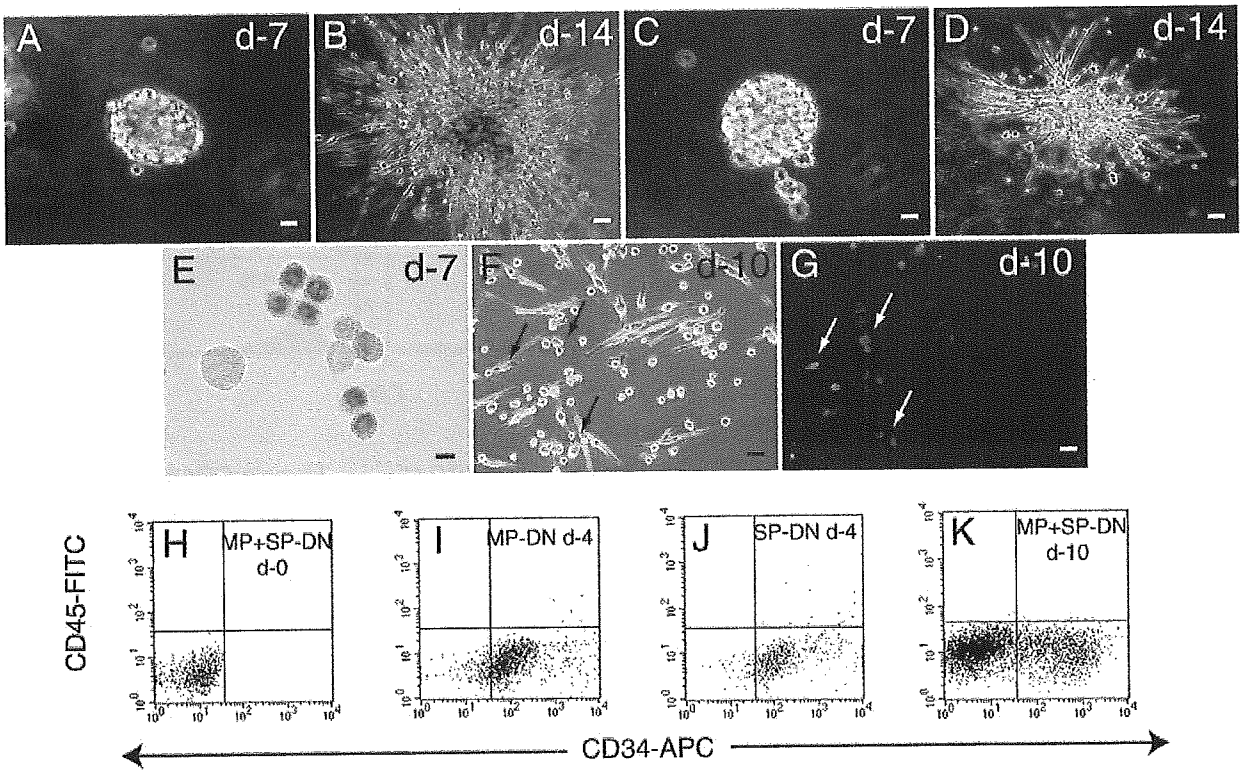

Fig. 3. Growth and differentiation of MP-DN and SP-DN cells in vitro. Colonies derived from MP-DN (A, B, E–G), and SP-DN (C, D) in collagen culture containing bFGF and EGF are depicted. DN cells in both populations typically formed sphere-like colonies at 7 days of culture (A, C). These spheres gradually increased in diameter and finally formed numerous myotubes at 14 d (B, D). When the spheres in A and C were resuspended in collagenase and subjected to cytospin and MyoD staining, about 60% of cells were positive for MyoD (E, brown). Adherent cells were also observed in the colonies (F), as they were in the Sk-34 colonies, and some cells demonstrated uptake of DiI-Ac-LDL at 10 days of culture (G, arrows). Interestingly, when the cells in the 4-day cultures were resuspended and analyzed by flow cytometry using CD34 and CD45 antigens, a lot of cells in both MP-DN and SP-DN cells expressed CD34 (I, J), and the relative number of CD34+ cells decreased after 10 days of culture (K). Note that there were no CD34−/45+ cells, and very few cells were observed in CD34+/45+ fraction. For comparison, the characteristics of total DN cells immediately after sorting (before culture) were shown in H. Colony-forming activity (%) in MP-DN and SP-DN cells was 9.8 ± 0.07 and 9.7 ± 0.2, respectively. Bars in A–G = 10 μm.

We also observed several cells that had an oil droplet-like structure (typical of fat cells) in the adhesive cell populations of MP- and SP-Sk-34 (Figs. 2P and T). The colony-forming activity was the same (1.6%) in both MP-Sk-34 and SP-Sk-34 populations.

Characteristics of DN cells

To assess the growth and differentiation potential of DN cell populations, we performed collagen-based clonal cell culture with bFGF and EGF (see Materials and methods) on purified MP-DN and SP-DN cells (Fig. 3). Both MP-DN (Fig. 3A) and SP-DN (Fig. 3C) cells formed sphere-like colonies after 4–7 days of culture. The diameter of these spheres gradually increased, and the colonies formed numerous myotubes after 14 days of culture (Figs 3B and D). The spheres were tested for MyoD expression by resuspension in collagenase and subjected to cytospin preparation and staining for MyoD. At 4–5 days of culture, a few MyoD+ cells were observed (data not shown). After 7 days, a majority of cells expressed MyoD (Fig. 3E). Adherent cells were also observed in DN cell culture at 10 days, as in Sk-34 culture, and these cells demonstrated DiI-Ac-LDL uptake (Figs. 3F and G, arrows). In addition, when total cells in DN cell culture was resuspended by collagenase and trypsin/EDTA and analyzed by flow cytometry using CD34 and CD45 at 10 days, there were totally CD45 negative (Fig. 3K). Interestingly, the colony-forming activity of DN cells were about 6-fold higher than that of Sk-34 cells (about 10% both in MP-DN and SP-DN cells, while 1.6% in Sk-34). After 4 days of culture, when the cells were resuspended and stained for CD34 and CD45, over 86% of DN cells from both the MP and SP fractions expressed CD34 (Figs. 3I and J). The proportion of cells expressing CD34 was lower at 10 days of culture (Fig. 3K), while an increase in the MyoD-positive population was observed around this time (Fig. 3E).

Expression of CD73 in the bone marrow cells, Sk-34, DN, and CD45+ fractions

To test the possibility that the Sk-34 and DN cells include bone marrow-derived stromal cells, these cells were stained by CD73 as well as Sca-1 (Fig. 4). In this respect,

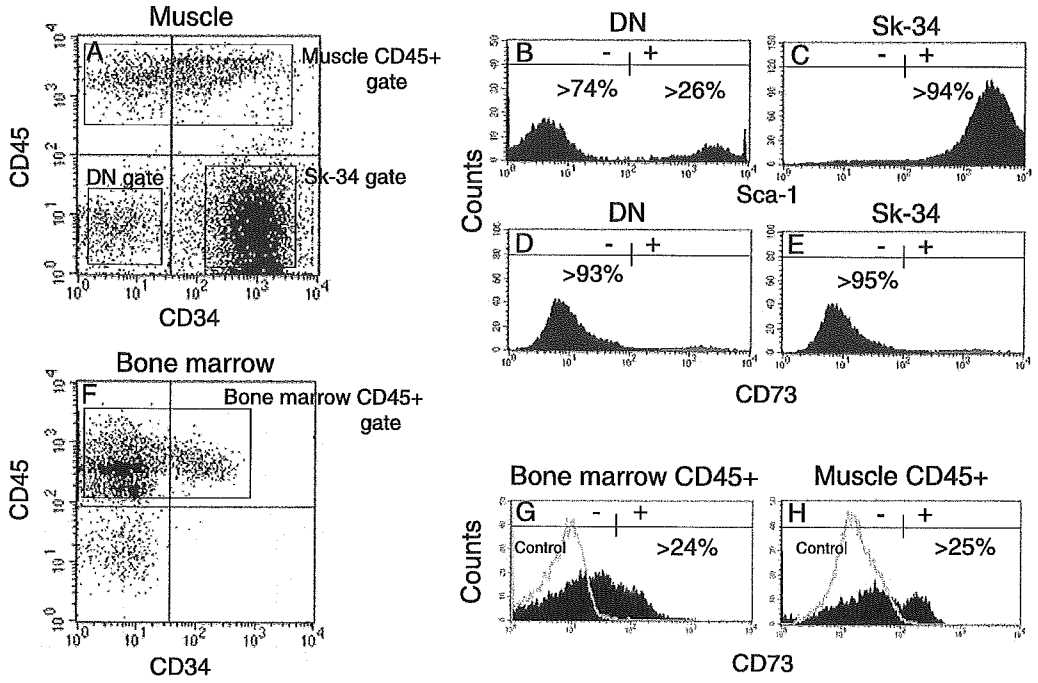

Fig. 4. Isolation and characterization of Sk-34, DN, and CD45+ cell populations. Shown are the basic sorting patterns of muscle-derived cells (A), and bone marrow-derived mononuclear cells (F). Fractions, enclosed by squares in A and F were further characterized by Sca-1 (B, C) and CD73 (D–H). Both Sk-34 and DN cells were >94% (C) and >26% (B) positive for Sca-1 and >95% (E) and >93% (D) negative for CD73. The skeletal muscle-derived CD45+ fraction contained >25% CD73+ cells (H). Similarly, bone morrow-derived CD45+ cells were >24% positive for CD73 (G).

we used nucleated whole bone marrow cells for positive control of CD73 analysis. Basic sorting patterns of EECs and bone marrow cells are shown in Figs. 4A and F. Analyzed gates of Sk-34, DN and CD45+ cell fractions in the muscle and CD45+ fraction in the bone marrow cells were enclosed by squares and further characterized by Sca-1 and CD73. Both Sk-34 and DN cells were >94% (C) and >26% (B) positive for Sca-1 and >95% (E) and >93% (D) negative for CD73, respectively. In contrast, skeletal muscle-derived CD45+ fraction contained >25% CD73+ cells (H). Similarly, bone morrow-derived CD45+ cells were >24% positive for CD73 (G).

Discussion

In the present study, we found that EECs include a very small SP cell population (0.08%), but are composed mostly of MP cells. Both in MP and in SP, cell populations were divided into four subpopulations: CD34−/45+, CD34+/45+, CD34+/45−, and CD34−/45−, and the patterns wholly corresponded to the total EEC sorting pattern that we recently reported [8]. About 58% of SP cells were present in the CD34+/45− (Sk-34) fraction, 36% in the CD34−/45− (DN) fraction, and the remaining 6% were CD45+ fractions. This result concurs with our previous report that the expression of Bcrp1/ABCG2 mRNA was detectable both in Sk-34 and in DN cell fractions [8]. SP-Sk-34 and MP-Sk-34 cells showed the same growth characteristics and multilineage differentiation to myogenic, endothelial, and fat cells. All of these characteristics in MP- and SP-Sk-34 cells correspond well with the characteristics of total Sk-34 cells, as reported previously under the same culture conditions [8]. However, the number of MP-Sk-34 cells was about 1000-fold higher than that of SP-Sk-34 and the colony-forming activity was the same in both populations. Thus, we conclude that the reported characteristics of Sk-34 cells [8] are primarily (99.9%) attributable to MP-Sk-34 cells. Additionally, the majority of floating and/or weakly attached cells after 10 days of culture were strongly or weakly positive for MyoD (Figs. 2I and J). Expression of MyoD was relatively low in larger cells. However, a few cells, typically smaller cells, still expressed CD34 while coexpressing MyoD (Figs. 2K and L). This clearly indicated that CD34+ cells differentiated into myogenic cells following an increase in their size and the disappearance of CD34 antigen.

As we have previously reported, the DN cell populations did not grow well under the culture conditions used for Sk-34 cells [8]. However, the DN cell populations also contained 0.06% of SP cells (Figs. 1C and D). To assess the growth and differentiation potential of MP-DN and SP-DN cell populations, we performed collagen-based clonal cell culture with bFGF and EGF (see Materials and methods). Importantly, when the DN cells were cultured without bFGF and EGF, the CFU with multilineage did not appear. The growth and differentiation characteristics of MP-DN and SP-DN cells were also identical in the collagen-based

culture medium. Both MP-DN and SP-DN cells formed sphere-like colonies after 4–7 days of culture (Figs. 3A and C). Spheres at Day 7 included MyoD-positive cells (Fig. 3E) and gradually increased their diameter and formed numerous myotubes after 14 days of culture (Figs. 3B and D). After 10 days of culture, adherent cells demonstrated DiI-Ac-LDL uptake (Figs. 3F and G), and when the total cells were resuspended from DN cell cultures, there were totally CD45 negative (Fig. 3K). These results indicate that the DN cells were also able to differentiate into myogenic and endothelial cells. Interestingly, the colony-forming activity of DN cells was about 6-fold higher than that of Sk-34 cells (about 10% in DN and 1.6% in Sk-34). Additionally, over 86% of DN cells in both the MP and the SP fractions expressed CD34 after 4 days of culture (Figs. 3I and J). The fraction of cells expressing CD34 decreased at 10 days of culture (Fig. 3K), while the fraction of MyoD-positive cells increased around this time (Fig. 3E). Taken together, these results suggest that DN cells differentiate into myogenic and endothelial cells through the expression of CD34 antigen. However, the functional relationship between Sk-34 and DN cells in vivo is still not clear. More importantly, these results clearly indicate that expression of CD34 antigen precedes MyoD expression during the myogenic process.

It is thought that the myogenic lineage-positive cells in Sk-34 and DN populations are derived from bone marrow stromal cells and remained in the interstitial spaces of skeletal muscle because muscle regeneration by bone marrow-derived myogenic progenitors has been suggested by Ferrari et al. [3]. Recently, it was also suggested that CD73 (ecto-5′-nucleotidase) may play a role in bone marrow stromal interactions and in the differentiation of mesenchymal stem cells, and that it is a possible marker for mesenchymal stem cells [15]. Based on this report, we performed CD73 staining to Sk-34, DN, and CD45+ cell populations. The results showed that both Sk-34 and DN cell populations were over 93–95% negative for CD73 (Figs. 4D and E). Thus, the possibility that Sk-34 and DN cell populations are derived from bone marrow stromal cells was low. In addition, CD73 was also found on endothelial cells in the thymus and peripheral lymphoid organs [16]. In this respect, both Sk-34 and DN cell populations include very few endothelial cells immediately after sorting, as we have reported previously [8]. Furthermore, over 94% of Sk-34 and 26% of DN cells were Sca-1 positive (Figs. 4B and C). These results indicate that over 80% of EECs were Sca-1 positive. Given the results shown in Figs. 1D, 4B, and 4C, it is likely that the muscle SP cell population that we sorted in the present study was mostly CD34+/−, CD45−, and Sca-1+. These results correspond to those of Gussoni et al. [5], who suggested that muscle SP cells are CD34+/−, Sca-1+, and CD45−. Interestingly, CD45+ fractions were >25% positive for CD73 (Fig. 4H). A recent bone marrow transplantation study has been interpreted to suggest that hematopoietic progenitors in the skeletal muscle have a bone marrow origin [17]. Similarly, two groups demonstrated that CD45+ cells in the skeletal muscle had hematopoietic stem cell activity [18,19]. Thus, it is reasonable to speculate that the CD45+ fractions in the skeletal muscle include hematopoietic progenitors and these cells were bone marrow in origin. In fact, we have also detected several hematopoietic colonies in the CD45+ cell population in muscle using clonal cell culture appropriately stimulated by several factors (data not shown). Therefore, cells in the CD45+ fractions in the skeletal muscle may have a unique multilineage differentiation potential when compared to Sk-34 and DN cells. However, it seems consistent that the skeletal muscle-derived CD45− cells were highly myogenic, whereas CD45+ cells displayed limited myogenic activity [19]. The relationship between satellite cells, Sk-34, and DN cells still remain unclear, and we are currently investigating these questions further.

Based on these observations, we conclude that the growth characteristics and multilineage differentiation were identical in skeletal muscle-derived MP and SP cells in clonal cell culture. However, the Sk-34 cells include only a few SP cells (<0.1%), and are wholly composed (99.9%) of an MP cell population. The CFU of DN cells can differentiate into myogenic and endothelial cells as well as Sk-34 cells, and these cells express CD34 antigen preceding MyoD expression during the myogenic process. These findings may provide new strategy for muscle tissue reconstitution therapy by defining a new source of stem cells that can be obtained more easily, rapidly, and effectively from skeletal muscle.

Acknowledgments

The authors thank Miss Hiroko Kouike (Keio University School of Medicine) for technical assistance with cell sorting. This work was supported by a Grant-in-Aid-for Scientific Research (14658234) from the Ministry of Education, Science, and Culture of Japan, and by Tokai University School of Medicine Research Aid.

References

[1] C.B. Johansson, S. Momma, D.L. Clarke, M. Risling, U. Lendahl, J. Frisen, Identification of a neural stem cell in the adult mammalian central nervous system, Cell 96 (1999) 25–34.
[2] B.A. Reynolds, S. Weiss, Generation of neurons and astrocytes from isolated cells of the adult mammalian central nervous system, Science 255 (1992) 1707–1710.
[3] G. Ferrari, G. Cusella-De Angelis, M. Coletta, E. Paolucci, A. Stornaiuolo, G. Cossu, F. Mavilio, Muscle regeneration by bone marrow-derived myogenic progenitors, Science 279 (1998) 1528–1530.
[4] D.J. Prockop, Marrow stromal cells as stem cells for nonhematopoietic tissues, Science 276 (1997) 71–74.
[5] E. Gussoni, Y. Soneoka, C.D. Strickland, E.A. Buzney, M.K. Khan, A.F. Flint, L.M. Kunkel, R.C. Mulligan, Dystrophin expression in the mdx mouse restored by stem cell transplantation, Nature 401 (1999) 390–394.

[6] K.A. Jackson, T. Mi, M.A. Goodell, Hematopoietic potential of stem cells isolated from murine skeletal muscle, Proc. Natl. Acad. Sci. USA. 96 (1999) 14482–14486.
[7] P. Seale, L.A. Sabourin, A. Girgis-Gabardo, A. Mansouri, P. Gruss, M.A. Rudnicki, Pax7 is required for the specification of myogenic satellite cells, Cell 102 (2000) 777–786.
[8] T. Tamaki, A. Akatsuka, K. Ando, Y. Nakamura, H. Matsuzawa, T. Hotta, R.R. Roy, V.R. Edgerton, Identification of myogenic-endothelial progenitor cells in the interstitial spaces of skeletal muscle, J. Cell Biol. 157 (2002) 571–577.
[9] T. Asahara, T. Murohara, A. Sullivan, M. Silver, R. van der Zee, T. Li, B. Witzenbichler, G. Schatteman, J.M. Isner, Isolation of putative progenitor endothelial cells for angiogenesis, Science 275 (1997) 964–967.
[10] T. Asahara, T. Takahashi, H. Masuda, C. Kalka, D. Chen, H. Iwaguro, Y. Inai, M. Silver, J.M. Isner, VEGF contributes to postnatal neovascularization by mobilizing bone marrow-derived endothelial progenitor cells, EMBO J. 18 (1999) 3964–3972.
[11] J. Yamashita, H. Itoh, M. Hirashima, M. Ogawa, S. Nishikawa, T. Yurugi, M. Naito, K. Nakao, Flk1-positive cells derived from embryonic stem cells serve as vascular progenitors, Nature 408 (2000) 92–96.
[12] S. Zhou, J.D. Schuetz, K.D. Bunting, A.M. Colapietro, J. Sampath, J.J. Morris, I. Lagutina, G.C. Grosveld, M. Osawa, H. Nakauchi, B.P. Sorrentino, The ABC transporter Bcrp1/ABCG2 is expressed in a wide variety of stem cells and is a molecular determinant of the side-population phenotype, Nature Med. 7 (2001) 1028–1034.
[13] R. Bischoff, Proliferation of muscle satellite cells on intact myofibers in culture, Dev. Biol. 115 (1986) 129–139.
[14] M.A. Goodell, K. Brose, G. Paradis, A.S. Conner, R.C. Mulligan, Isolation and functional properties of murine hematopoietic stem cells that are replicting in vivo, J. Exp. Med. 183 (1996) 1797–1806.
[15] F. Barry, R. Boynton, M. Murphy, J. Zaia, The SH-3 and SH-4 antibodies recognize distinct epitopes on CD73 from human mesenchymal stem cells, Biochem. Biophys. Res. Commun. 289 (2001) 519–524.
[16] Y. Yamashita, S.W. Hooker, H. Jiang, A.B. Laurent, R. Rest, K. Khare, A. Coe, P.W. Kincade, L.F. Thompson, CD73 expression and fyn-dependent signaling on murine lymphocytes, Eur. J. Immunol. 28 (1998) 2981–2990.
[17] H. Kawada, M. Ogawa, Bone marrow origin of hematopoietic progenitors and stem cells in murine muscle, Blood 98 (2001) 2008–2013.
[18] A. Asakura, P. Seale, A. Girgis-Gabardo, M.A. Rudnicki, Myogenic specification of side population cells in skeletal muscle, J. Cell Biol. 159 (2002) 123–134.
[19] S.L. Mckinney-Freeman, K.A. Jackson, F.C. Camargo, G. Ferrari, F. Mavilio, M.A. Goodell, Muscle-derived hematopoietic stem cells are hematopoietic in origin, Proc. Natl. Acad. Sci. USA 99 (2002) 1341–1346.

THE JOURNAL OF BIOLOGICAL CHEMISTRY
Vol. 278, No. 42, Issue of October 17, pp. 41309–41315, 2003
Printed in U.S.A.

Origin of Higher Affinity to RNA of the N-terminal RNA-binding Domain than That of the C-terminal One of a Mouse Neural Protein, Musashi1, as Revealed by Comparison of Their Structures, Modes of Interaction, Surface Electrostatic Potentials, and Backbone Dynamics*

Received for publication, June 12, 2003, and in revised form, August 5, 2003
Published, JBC Papers in Press, August 7, 2003, DOI 10.1074/jbc.M306210200

Youhei Miyanoiri‡, Hisanori Kobayashi‡,, Takao Imai§, Michinao Watanabe‡, Takashi Nagata‡, Seiichi Uesugi‡, Hideyuki Okano§, and Masato Katahira‡¶

From the ‡Department of Environment and Natural Sciences, Graduate School of Environment and Information Sciences, Yokohama National University, 79-7 Tokiwadai, Hodogaya-ku, Yokohama 240-8501 and the §Department of Physiology, Keio University School of Medicine, 35 Shinanomachi, Shinjuku-ku, Tokyo 160-8582, Japan

Musashi1 is an RNA-binding protein abundantly expressed in the developing mouse central nervous system. Its restricted expression in neural precursor cells suggests that it is involved in maintenance of the character of progenitor cells. Musashi1 contains two ribonucleoprotein-type RNA-binding domains (RBDs), RBD1 and RBD2, the affinity to RNA of RBD1 being much higher than that of RBD2. We previously reported the structure and mode of interaction with RNA of RBD2. Here, we have determined the structure and mode of interaction with RNA of RBD1. We have also analyzed the surface electrostatic potential and backbone dynamics of both RBDs. The two RBDs exhibit the same ribonucleoprotein-type fold and commonly make contact with RNA on the β-sheet side. On the other hand, there is a remarkable difference in surface electrostatic potential, the β-sheet of RBD1 being positively charged, which is favorable for binding negatively charged RNA, but that of RBD2 being almost neutral. There is also a difference in backbone dynamics, the central portion of the β-sheet of RBD1 being flexible, but that of RBD2 not being flexible. The flexibility of RBD1 may be utilized in the recognition process to facilitate an induced fit. Thus, comparative studies have revealed the origin of the higher affinity of RBD1 than that of RBD2 and indicated that the affinity of an RBD to RNA is not governed by its fold alone but is also determined by its surface electrostatic potential and/or backbone dynamics. The biological role of RBD2 with lower affinity is also discussed.

In *Drosophila*, during sensory organ development, Notch signaling directs the asymmetry between neuronal and non-neuronal lineages (1), and a zinc finger transcriptional repressor, Tramtrack69, acts downstream of Notch as a determinant of non-neuronal identity (2, 3). *Drosophila musashi* was identified as a gene whose mutation causes a severe defect in the development of external sensory organs (4). It was demonstrated that the *Drosophila* Musashi protein represses the expression of the Tramtrack69 protein translationally in a neuronal lineage by binding to a *cis*-acting element in the 3′-untranslated region of *tramtrack69* messenger RNA (5, 6).

Also, in mammalian neural development, neural RNA-binding proteins play important roles by regulating gene expression post-transcriptionally. During mammalian central nervous system development, neurons and glial cells are thought to be generated from common neural precursor cells located in the periventricular area (7). Musashi1, a mammalian homologue of *Drosophila* Musashi, is expressed in the neural precursor cells that exist in the ventricular area of the developing mouse neural tube (6, 8), and it is expressed complementarily to another neural RNA-binding protein, Hu, a member of the Elav subfamily localized in differentiated neurons in the central nervous system (11–13). This combination of neural RNA-binding proteins might be important for cell fate determination in the developing central nervous system (14). Musashi1, which is evolutionally conserved in different species, may be required for the self-renewal and neuronal potential retention of neural stem cells in the developing mouse nervous system (6, 15), as judged from the analogy to its *Drosophila* homologue. In fact, it was demonstrated that Musashi1 translationally regulates the expression of a mammalian *numb* gene, which encodes a membrane-associated antagonist of Notch signaling, by interacting with *numb* mRNA (16).

Mouse Musashi1 consists of 362 residues and has two ribonucleoprotein (RNP)[1]-type RNA-binding domains (RBDs), RBD1 and RBD2 (8, 17). The RNP-type RBD is one of the most common eukaryotic protein sequence motifs (18), being found in hundreds of proteins (19–22). 46% of the amino acid sequence is identical between RBD1 and RBD2. When similar amino acids are taken into account, the homology reaches as high as 75%. Previously, we reported that RBD1 binds to poly(U) and poly(G), whereas the binding of RBD2 to RNA homopolymers was not detected under the same conditions (17). Then, the target sequences of mouse Musashi1 were de-

* This work was supported by Grants-in-aid for Scientific Research 12470487 and 15030214 and the Protein 3000 Project of the Ministry of Education, Culture, Sports, Science and Technology of Japan (to M. K.). The costs of publication of this article were defrayed in part by the payment of page charges. This article must therefore be hereby marked "*advertisement*" in accordance with 18 U.S.C. Section 1734 solely to indicate this fact.

The atomic coordinates and structure factors (code 1UAW) have been deposited in the Protein Data Bank, Research Collaboratory for Structural Bioinformatics, Rutgers University, New Brunswick, NJ (http://www.rcsb.org/).

¶ To whom correspondence should be addressed. Tel.: 81-45-339-4264; Fax: 81-45-339-4264; E-mail: masakata@ynu.ac.jp.

[1] The abbreviations used are: RNP, ribonucleoprotein; hnRNP, heterogeneous nuclear ribonucleoprotein; RBD, RNA-binding domain; NOE, nuclear Overhauser effect; NOESY, NOE spectroscopy; TOCSY, total correlation spectroscopy; HSQC, heteronuclear single-quantum coherence spectroscopy.

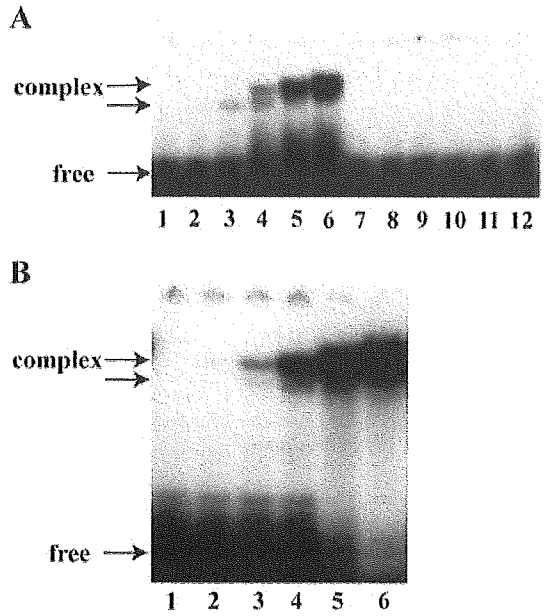

FIG. 1. **Gel retardation experiments as to RBD1, RBD2, and RBD1-RBD2.** As shown in *A*, 4 fmol of ^{32}P-labeled r(GUUAGUUAGUUAGUU) (T4-3) was incubated with 0, 1.5, 4.4, 13, 40, and 120 pmol of either RBD1 (*lanes 1–6*) or RBD2 (*lanes 7–12*). The mixtures were run on polyacrylamide gel. As shown in *B*, 4 fmol of ^{32}P-labeled T4-3 was incubated with 0, 0.008, 0.04, 0.2, 1, and 5 pmol of RBD1-RBD2 and run on polyacrylamide gel (*lanes 1–6*).

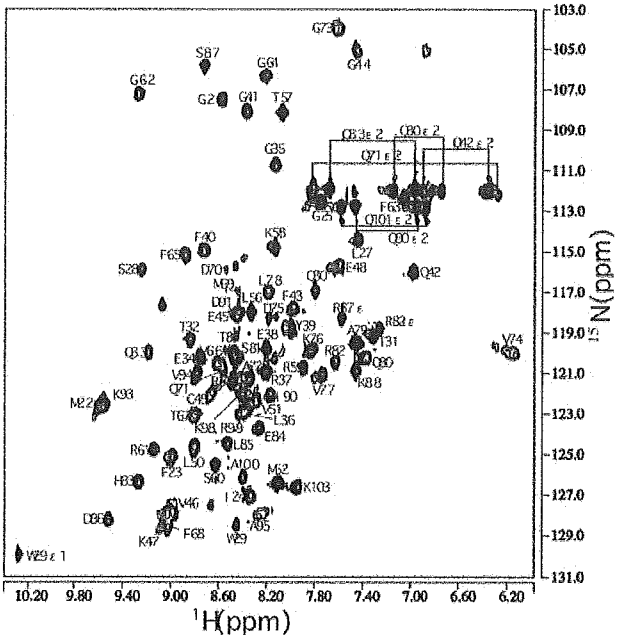

FIG. 2. **^{1}H-^{15}N HSQC spectrum of Musashi1 RBD1 at 25 °C and pH 6.0 with the assignments of H^N-N of the backbone, $H^{\varepsilon 2}$-$N^{\varepsilon 2}$ of Gln residues, and $H^{\varepsilon 1}$-$N^{\varepsilon 1}$ of a Trp residue.**

termined by the *in vitro* selection method (23, 24). (G/A)U$_n$AGU (n = 1–3) sequences were identified as consensus ones (16). Here, we report the gel retardation experiments indicating that RBD1 alone specifically binds to one of the target sequences, r(GUUAGUUAGUUAGUU) (T4-3), whereas such binding is not detected for RBD2 under the same conditions.

We reported the structure and qualitative analysis of the backbone dynamics of RBD2 (25). Additionally, we succeeded in detecting the binding of RBD2 to the target RNA and in characterizing the mode of interaction by NMR (25). Here, to elucidate the origin of the much higher affinity of RBD1 to RNA than that of RBD2 and the basis of the recognition of the target RNA, we have determined the structure and mode of interaction with RNA of RBD1. We have also compared the surface electrostatic potentials of the interactive surface as to RNA for the two RBDs. Moreover, we have compared the backbone dynamics of the two RBDs by means of quantitative model-free analysis. These studies have indicated that the higher affinity to RNA is brought about by the positive surface potential of the interactive β-sheet and/or the flexibility of the central portion of the β-sheet.

EXPERIMENTAL PROCEDURES

Gel Retardation Experiments—Gel retardation experiments were performed as described previously (16). ^{32}P-labeled r(GUUAGUUAGUUAGUU) (T4-3) was incubated with various amounts of RBD1, RBD2, or their tandem link (RBD1-RBD2) at room temperature for 30 min. The complexes were run on a 15% polyacrylamide gel containing 0.5× Tris borate buffer and EDTA. The gels were then dried and exposed to XAR autoradiography film (Eastman Kodak Co.).

Sample Preparation for NMR—Escherichia coli BL21(DE3), transformed with a plasmid, pMMA, containing DNA encoding mouse Musashi1 RBD1-(20–103) was grown in M9 minimal medium with $^{15}NH_4Cl$ as a sole nitrogen source and then harvested. The cells were lysed by sonication. After purification with ammonium sulfate, RBD1 was loaded onto a DE52 anion-exchange column (Whatman), and then the flow-through fraction was loaded onto a HiTrap-SP cation-exchange column (Amersham Biosciences). The fraction eluted with NaCl was loaded onto a HiTrap-Q anion-exchange column (Amersham Biosciences), and the flow-through fraction was collected. RBD1 was dialyzed against 20 mM sodium phosphate (pH 6.0), 10 mM [$^2H_6$]dithiothreitol, and 1 mM NaN_3, and then concentrated to 2 mM using Centricon-3 (Amicon). RNA oligomers were prepared as described previously (25).

NMR Spectroscopy—NMR spectra were recorded with a Bruker DRX600 spectrometer equipped with a quadruple resonance probe with X, Y, and Z gradients. 2,2-Dimethyl-2-silapentane-5-sulfonate was used as an internal chemical shift reference. The following NMR experiments were performed to assign the resonances of RBD1 and to obtain distance and dihedral angle constraints: NOESY, TOCSY, double quantum filtered COSY, ^{15}N-edited NOESY-HSQC, ^{15}N-edited TOCSY-HSQC, and HNHA experiments. For titration experiments, a concentrated RNA solution was added step by step to the RBD1 solution, ^{1}H-^{15}N HSQC spectra being recorded at each step. Spectra were processed with XWIN-NMR (Bruker), Felix (MSI), NMRPipe (26), and Capp/Pipp/Stapp (27).

^{15}N T_1, T_2, and NOE spectra of RBD1 and RBD2 were recorded and processed as described previously (28). T_2 spectra were recorded at various protein concentrations, 2.0, 0.4, and 0.25 mM for RBD1 and 2, 0.6, and 0.3 mM for RBD2.

Structure Calculations—870 distance constraints (203 intraresidue, 254 sequential, 130 medium range, and 283 long range distance constraints) were obtained for RBD1 from NOESY and ^{15}N-edited NOESY-HSQC spectra, as described previously (25, 28, 29). Thirty-seven dihedral angle constraints for φ were obtained from an HNHA experiment. Eight dihedral angle constraints for χ_1 were also obtained, together with stereospecific assignment of the β-methylene protons of AM*X* and the γ-methyl protons of valine residues. Additionally, in the later stage of the calculations, 42 distance constraints for 21 hydrogen bonds were included for slowly exchanging amide protons within the identified secondary structure elements.

Structure calculations were carried out using distance and dihedral angle constraints with a simulated annealing protocol supplied with X-PLOR v. 3.8 (30). A final set of 15 structures was selected from 100 calculations on the basis of the criteria of the smallest residual energy values. None of them violated the distance constraints by more than 0.4 Å or dihedral angle constraints by more than 4°. A mean structure was obtained by averaging the coordinates of the 15 structures, and a restrained energy minimized mean structure was obtained by energy minimization of the mean structure under the constraints. The quality of the structures was evaluated with PROCHECK (31).

Surface Electrostatic Potentials and Backbone Dynamics—The surface electrostatic potentials of RBD1 and RBD2 were calculated with GRASP (32). The backbone dynamics of RBD1 and RBD2 were quanti-

TABLE I
Structural statistics for RBD1 of Musashi1

	15 refined structures
X-PLOR energies (kcal/mol)	
E_{total}	288 ± 11
E_{bond}	15 ± 1
E_{angle}	140 ± 6
$E_{improper}$	19 ± 1
E_{vdw}	28 ± 3
E_{NOE}	85 ± 5
E_{cdih}	0.47 ± 0.25
r.m.s.d.[a] from idealized geometry	
Bonds (Å)	0.0033 ± 0.0001
Angles (deg.)	0.610 ± 0.013
Impropers (deg.)	0.421 ± 0.013
r.m.s.d. from experimental constraints	
Distances (Å)	0.043 ± 0.001
Dihedral angles (degrees)	0.403 ± 0.101
NOE violations	
Number of violations greater than 0.4 Å	0 ± 0
Dihedral angle violations	
Number of violations greater than 4 degrees	0 ± 0
Ramachandran analysis for 21–95 region residues	
In most favored regions (%)	58.8
In additional favored regions (%)	33.7
In generously allowed regions (%)	6.4
In disallowed regions (%)	1.1
r.m.s.d. of 15 refined structures *versus* mean structure (Å) for 21–95 region excluding loop 3 (53–62) and loop 4 (69–71)	
Backbone atoms (Å)	0.49 ± 0.10
All heavy atoms (Å)	0.95 ± 0.11

[a] r.m.s.d., root mean square deviation.

tatively analyzed by model-free analysis of the relaxation data (33), as described previously for another RBD (28). The Modelfree program was used (34).

RESULTS

Difference in RNA Binding Activity among RBD1, RBD2, and RBD1-RBD2—RNA binding activities of RBD1, RBD2, and their tandem link with a native linker (RBD1-RBD2) were examined by gel retardation experiments. r(GUUAGUUAGUUAGUU) (T4-3), which was obtained as one of the target sequences by means of the *in vitro* selection method (16), was used for the examination. T4-3 comprises at least two consensus sequences, (G/A)U_nAGU (n = 1–3), tandemly, and even three if overlapping is allowed. T4-3 was incubated with RBD1, RBD2, or RBD1-RBD2 and run on the gel. Binding of RBD1 to T4-3 was observed, whereas that of RBD2 was not detected under the experimental conditions applied (Fig. 1*A*). From the densitometric analysis of the results, the dissociation constant for the RBD1-RNA complex was determined to be 3–9 μM. Binding of RBD1-RBD2 to T4-3 was also observed (Fig. 1*B*), and the dissociation constant was determined to be 40–88 nM.

Resonance Assignments and Structure Calculations for RBD1—Sequential assignments of the main chain and side chain ^{1}H and ^{15}N resonances of RBD1 were made in the same way as reported for RBD2 (25). The assignments of the main chain H^N and N resonances, together with those of $H^{\epsilon 2}$ and $N^{\epsilon 2}$ of Gln residues and $H^{\epsilon 1}$ and $N^{\epsilon 1}$ of a Trp residue, are presented in Fig. 2.

The structures of RBD1 were calculated on the basis of distance and dihedral angle constraints. The structural statistics are shown in Table I. The backbone root mean square deviation of the 15 final structures *versus* the mean structure was 0.49 ± 0.10 Å for the 21–95 region, excluding less well defined loop 3 (53–62) and loop 4 (69–71).

Structure of RBD1—Fig. 3*A* shows a stereo view of superposition of the 15 final structures of RBD1. Fig. 3*B* shows a stereo view of the restrained energy minimized mean structure of RBD1. RBD1 exhibits typical RNP-type fold, a four-stranded antiparallel β-sheet (β1, Lys-21–Gly-25; β2, Val-46–Met-52; β3, Phe-63-Phe-68; and β4, Asp-91–Ala-95) packed against two α-helices (α1, Gln-33–Phe-43; and α2, Ala-72–Ala-79), as observed for RBD2 (Fig. 3*C*) (25). Additionally, a short antiparallel β-sheet (Glu-84–Leu-85:Lys-88–Thr-89) was identified in loop 5 located between α2 and β4. A similar short β-sheet was identified for the other RNP-type RBDs of hnRNP D0 (28, 29). A β-bulge structure was found in the Val-46–Glu-48 region of β2, which is common to most RNP-type RBDs. Phe-23, Phe-63, and Phe-65 of RBD1 form a hydrophobic patch exposed to the solvent, as observed for Phe-112, Phe-152, and Phe-154 of RBD2 (Fig. 3, *B* and *C*). The backbone root mean square deviation between RBD1 and RBD2 for the β1 to β4 region, which is shown in Fig. 3, was 2.2 Å, excluding loop 3. It should be added that the right-handed twist of the β1- and β3-strands of RBD1 is slightly greater than that in the case of RBD2.

The Mode of Interaction with RNA of RBD1—Fig. 4*A* shows chemical shift perturbations of RBD1 on binding of one of the target sequences identified through *in vitro* selection, r(GUUAGUUAGUUAGUU) (16). For comparison, those of RBD2 are shown in Fig. 4*B*. The perturbations were observed on the β-sheet side, not on the opposite side composed of two α-helices. Residues interacting with RNA or present near the binding interface are expected to exhibit relatively large perturbations. It is apparent that the interaction with RNA takes place on the β-sheet side of RBD1 as in the case of RBD2.

Although the binding of RBD2 to RNA was not detected in gel retardation experiments (Fig. 1*A*), it was detected with NMR (25). This is explained by the fact that higher RBD2 and RNA concentrations and the absence of salts and a detergent for NMR experiments facilitate the formation of the complex (25). In this sense, NMR is a suitable method for the characterization of a weak interaction that is hard to detect by means of biochemical methods.

Comparison of Surface Electrostatic Potentials between RBD1 and RBD2—The surface electrostatic potential of the β-sheet side, which interacts with RNA, was calculated for RBD1 and RBD2 and compared (Fig. 5). Notably, the β-sheet surface of RBD1 is entirely positively charged, whereas that of

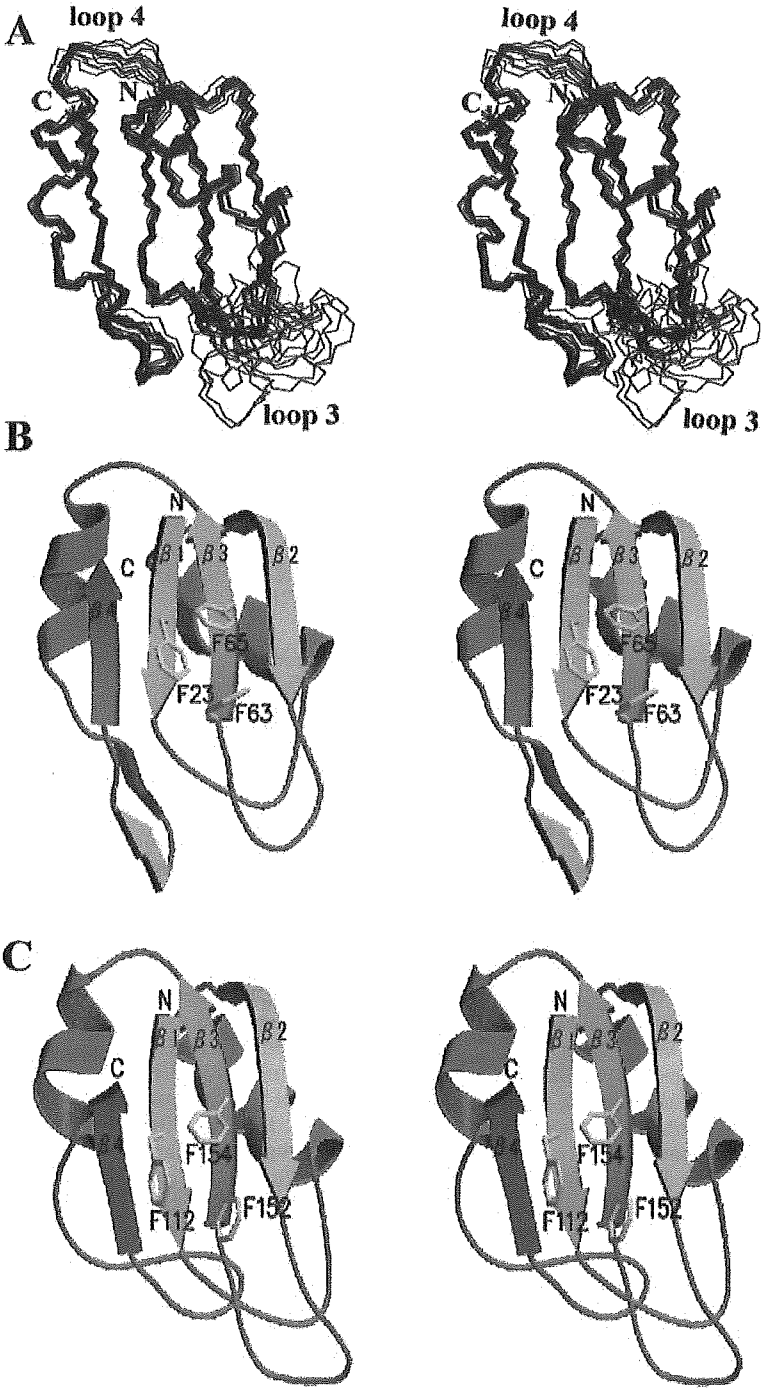

FIG. 3. **The structures of Musashi1 RBDs.** *A*, a stereo view of superposition of the main chains of 15 final structures. *N* and *C* indicate Lys-21 and Ala-95, respectively, and loops 3 and 4 are labeled. *B*, a stereo view of the main chain of a restrained energy minimized mean structure of RBD1. α-Helices and β-strands are colored *red* and *cyan*, respectively. The side chains of Phe-23, Phe-63, and Phe-65 are also shown. *C*, a stereo view of the main chain of a restrained energy minimized mean structure of RBD2 from Ref. 25. *N* and *C* indicate Lys-110 and Ala-184, respectively. The side chains of Phe-112, Phe-152, and Phe-154 are also shown.

RBD2 is largely neutral. It was confirmed that these characters are seen for all final structures of RBD1 and RBD2. RNA is negatively charged due to phosphate groups. Thus, from the viewpoint of electrostatic interactions, RBD1 is expected to bind RNA more strongly than RBD2.

Backbone Dynamics of RBD1 and RBD2—To shed light from a dynamical point of view on the recognition of RNA by Musashi1, the backbone dynamics of RBD1 and RBD2 were analyzed quantitatively, in the same way as described in detail for another RNP-type RBD (28). Examination of the concentration-dependence of the ^{15}N T_2 value confirmed that RBD1 and RBD2 are in a monomeric form at the protein concentrations of 0.4 and 0.6 mM, respectively. Model-free analysis was performed for relaxation data recorded at these concentrations.

First, it was found that an axially symmetric diffusion model can well describe the overall rotational diffusion of both RBD1 and RBD2. Three relaxation data, $R_1(= 1/T_1)$, $R_2(= 1/T_2)$, and NOE, were fitted for each RBD with five models consisting of the following subsets of extended model-free parameters: 1) S^2; 2) S^2 and τ_e; 3) S^2 and R_{ex}; 4) S^2, τ_e, and R_{ex}; and 5) S_f^2, S^2, and τ_e, where S^2 is the square of a generalized order parameter, τ_e an effective correlation time, R_{ex} is a chemical exchange term,

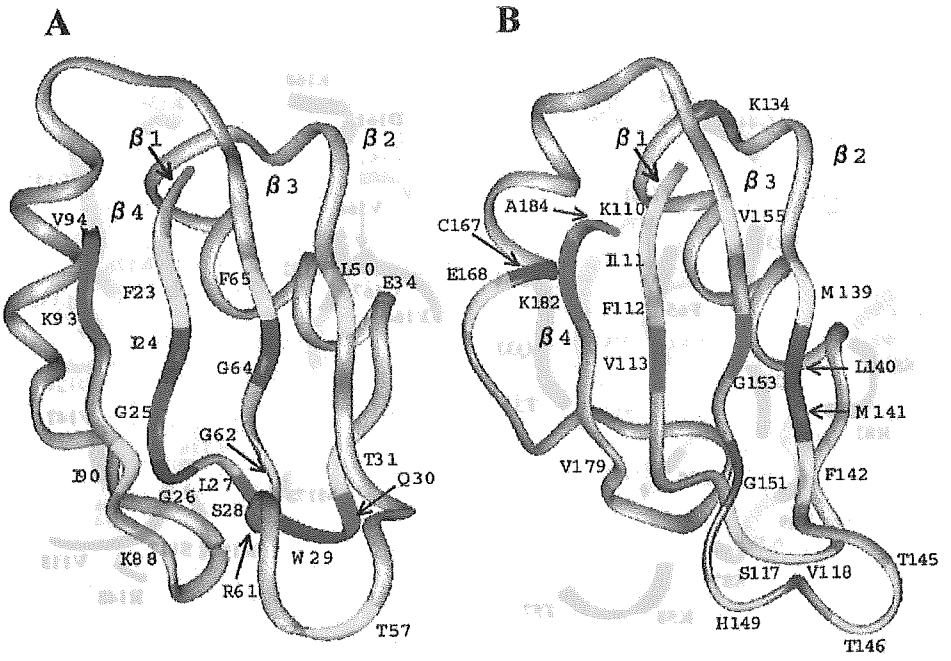

FIG. 4. **Mapping of chemical shift perturbations upon binding of the target RNA.** The residues with combined chemical shift perturbations as to H^N and N (absolute values) of >125 and 75–125 Hz are colored *red* and *yellow*, respectively, and those whose ^1H-^{15}N correlation peaks disappeared are colored *blue*. *A*, Musashi1 RBD1; *B*, RBD2 from Ref. 25.

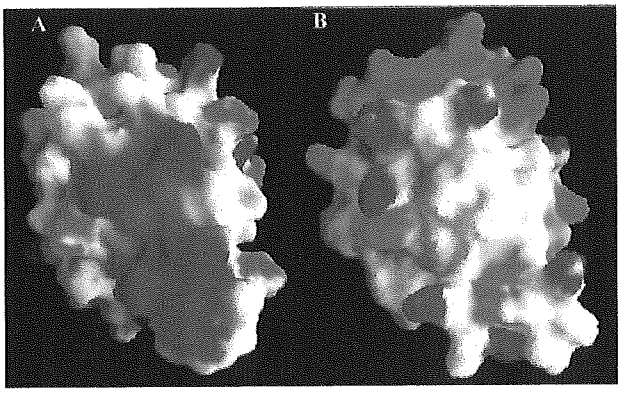

FIG. 5. **The surface electrostatic potential.** *A*, Musashi1 RBD1; *B*, RBD2. Positive surface potential > $+5K_BT$ and negative surface potential < $-5K_BT$ are represented in *blue* and *red*, respectively, where K_B is the Boltzmann constant and T is the absolute temperature.

and S_f^2 is the square of an order parameter for an internal motion on a fast time scale (28, 33–36). The numbers of residues fitting each model were as follows for RBD1: 1) 10, 2) 5, 3) 12, 4) 25, and 5) 13 residues. Those for RBD2 were as follows: 1) 15, 2) 5, 3) 5, 4) 28, and 5) 10 residues.

The results of analyses of the backbone dynamics are summarized in Fig. 6, residues being mapped that require either a chemical exchange term, R_{ex}, greater than 1 s^{-1}, or a two-time scale spectral density function with a correlation time for slow internal motion, τ_s. R_{ex} and τ_s represent the flexibility on the milli- and pico- to nanosecond time scales, respectively. It is notable that the two central β-strands, β1 and β3, of RBD1 exhibit flexibility on either the milli- or pico- to nanosecond time scale, whereas those of RBD2 do not.

DISCUSSION

The mouse Musashi1 protein is drawing great attention because of its possible dominant role in regulation of the self-renewal and neuronal potential retention of neural stem cells in the developing nervous system (16). It is supposed that Musashi1 translationally regulates the expression of a certain gene such as *numb*, which is involved in Notch signaling, through interaction with mRNA of that gene (16). Musashi1 possesses two RBDs, RBD1 and RBD2. Despite the high sequence homology between them, RBD1 binds to target RNA much more strongly than RBD2. Here, we have elucidated the mechanism underlying the higher affinity of RBD1 to RNA. The study also suggests how Musashi1 is able to bind to the target RNA effectively.

Although a short antiparallel β-sheet has been detected exclusively for RBD1, a similar β-sheet-like structure has also been found for RBD2 (25). Thus, the fold is essentially identical for RBD1 and RBD2, a four-stranded antiparallel β-sheet being packed against two α-helices (Fig. 3, *B* and *C*). Either the Phe or Tyr residue is conserved at the positions of Phe-23 and Phe-65 of RBD1 (Phe-112 and Phe-154 of RBD2) in RNP-type RBDs (20, 21, 37). The stacking interactions of these residues of RNP-type RBDs with the bases of the target RNA are one of the major forces for the stabilization of a protein-RNA complex. In fact, mouse Musashi1 and *Drosophila* Musashi with the mutation of these residues cannot bind to RNA (5, 16). Although the orientations of the aromatic rings of Phe-23 and Phe-65 of RBD1 are somehow different from those of Phe-112 and Phe-154 of RBD2, all of these rings are exposed to the solvent for the achievement of the stacking interactions with bases on the β-sheet.

A slightly greater right-handed twist of the β1- and β3-strands was observed for RBD1 in comparison with that of RBD2. We noticed a similar difference between RBD1 and RBD2 of an RNP-type U1A protein on inspection of their structures deposited in the Protein Data Bank. It is interesting that in the cases of both proteins, RBD1, which exhibits higher affinity to RNA, exhibits a slightly greater right-handed twist of the β1- and β3-strands. The greater twist of these β-strands may be favorable for amino acid residues to interact with RNA.

The mode of interaction with the target RNA is also identical for RBD1 and RBD2 of Musashi1 in the sense that the β-sheet

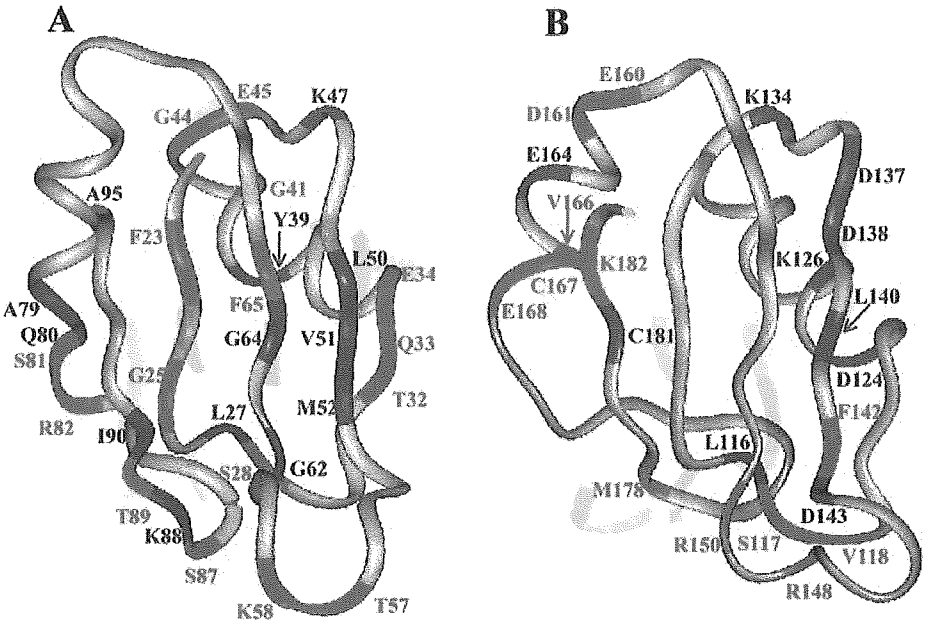

FIG. 6. **Mapping of the backbone dynamics.** The residues that require either a chemical exchange term, R_{ex}, greater than 1 s^{-1}, or a two-time scale spectra density function with a correlation time for slow internal motion, τ_s, are colored *red* and *blue*, respectively. *A*, Musashi1 RBD1; *B*, RBD2.

is the interactive surface (Fig. 4, *A* and *B*). Thus, studies on the protein fold and mode of interaction with RNA have left the origin of the higher affinity of RBD1 to RNA to be answered largely from different viewpoints.

It is notable that the surface electrostatic potential of the β-sheet, which interacts with RNA, differs drastically between RBD1 and RBD2, despite the essentially identical fold (Fig. 5, *A* and *B*). The positive surface potential is prevailing for the β-sheet side of RBD1. On the other hand, the surface potential of the β-sheet side of RBD2 is largely neutral, and even the negative surface potential has been found for some portions. Apparently, the electrostatic character of RBD1 is favorable for the binding of negatively charged RNA as compared with that of RBD2. Thus, the higher affinity of RBD1 to RNA can be accounted for from the electrostatic viewpoint of the interactive surface.

The amino acid residues that contribute to the formation of the positive surface for the β-sheet side of RBD1 are mostly conserved in RBD2. In the case of RBD1, the side chains of basic residues, Arg and Lys, are located on the β-sheet, where they form a large positive surface area, those of acidic residues, Asp and Glu, being spread away from the β-sheet without disturbing the positive surface. In the case of RBD2, on the other hand, the side chains of basic residues are spread away from the β-sheet, and those of some acidic residues are located on the β-sheet, which results in the mostly neutral and even partially negative surface of the β-sheet. In this way, the drastic difference in the surface electrostatic potential arises.

A remarkable difference between RBD1 and RBD2 of Musashi1 was also noticed in dynamics. In particular, the central two β-strands, β1 and β3, of RBD1 exhibit flexibility on either the milli- or pico- to nanosecond time scale, whereas those of RBD2 do not (Fig. 6, *A* and *B*). The two Phe residues (Phe-23 and Phe-65 of RBD1 and Phe-112 and Phe-154 of RBD2) located in β1 and β3, respectively, undergo key stacking interactions with RNA bases, as described earlier. Thus, the flexibility of RBD1 may be utilized in the recognition process because it allows different conformational states to be accessed and facilitates an induced fit. In fact, the utilization of flexibility in recognition has been reported for other RNP-type RBDs, U1A and hnRNP D (28, 38). Thus, the flexibility of Musashi1 RBD1 may be favorable for the induction of ideal mutual positioning for strong stacking between the aromatic rings of the Phe residues and RNA bases. The flexibility of RBD1 may also be utilized by other residues to interact with RNA. On the other hand, the lack of flexibility of the β1- and β3-strands of Musashi1 RBD2 may restrict the induction of ideal mutual positioning of the Phe rings and RNA bases, which may result in weaker binding. The chemical shift perturbations of Phe-23 and Phe-65 of RBD1 are large, ~80 and 110 Hz, respectively. Although the perturbation of Phe-112 of RBD2 is relatively large, ~75 Hz, that of Phe-154 of RBD2 is rather small, ~30 Hz. These results seem to be consistent with the idea of the better stacking for RBD1, although the backbone NH group, which is located relatively far from the side chain aromatic ring, is occasionally not a good indicator as to stacking interactions (28). Thus, the higher affinity of RBD1 to RNA can also be rationalized from a dynamical viewpoint.

The β1- and β3-strands approximately correspond to the RNP2 hexamer and RNP1 octamer sequences, respectively, both of which are highly conserved in RNP-type RBDs. Therefore, the difference in flexibility of the β1- and β3-strands between the two RBDs is not brought about by the sequence difference, but is supposed to originate from the global character of the proteins.

r(GUUAGUUAGUUAGUU) (T4-3) comprises at least two consensus sequences, (G/A)U_nAGU (n = 1–3), tandemly, and even three consensus sequences tandemly if overlapping is allowed. The chemical shift perturbation experiment to detect the interactions was also carried out with r(GUUAGUU), which only possesses a single consensus sequence. The perturbations obtained with r(GUUAGUU) were almost the same as those with r(GUUAGUUAGUUAGUU) (data not shown). This suggests that the binding of a single RBD can be achieved at a single consensus sequence.

Musashi1 binds to *numb* mRNA and translationally regulates the expression of the *numb* gene (16). The putative binding sequence of Musashi1 present in *numb* mRNA,

r(GUAGUAGU), is composed of two consensus sequences arranged tandemly in an overlapped way (16). When Musashi1 comprising both RBD1 and RBD2 binds to *numb* mRNA, it is supposed that RBD1 and RBD2 tandemly bind to the two consensus sequences, respectively. In this case, RBD1, the affinity of which to RNA is much higher than that of RBD2, may play a primary role in the binding. However, although the affinity of RBD2 to RNA is much lower, RBD2 may still be able to play a certain role. For example, even if the dissociation constant of an RBD2-RNA complex is 10^{-3} M, the joining of RBD2 to RBD1 theoretically could increase the affinity by 1000 times maximally. Actually, it was shown experimentally that the joining of RBD2 to RBD1 increased the affinity to T4-3 by ~100-fold (dissociation constants: 3–9 μM to 40–88 nM), as described previously. This increase in affinity may be necessary for the regulation of the *numb* gene by Musashi1. Thus, the contribution of RBD2 could potentially be critical. There is another possibility that if the affinity of RBD2 to RNA is as high as that of RBD1, Musashi1 may bind to *numb* mRNA too strongly for turn over. Thus, the lower affinity of RBD2 may be suitable for Musashi1 to exert a biological function. In this context, it was interesting to find that the affinity of RBD to RNA can be easily tuned by changing the surface electrostatic potential and/or the backbone dynamics, the fold itself remaining unchanged.

The assumption with a structural genomics approach is that the function of a protein can be deduced from its structure. This reminds us of the necessity of being aware that although the fold of RBD1 and RBD2 is essentially identical, their affinity to RNA is drastically different. To deduce the function of a protein, the surface electrostatic potential and backbone dynamics should also be considered, together with fold.

Acknowledgments—We thank Dr. Y. Kurihara and T. Ikeda for technical assistance.

REFERENCES

1. Jan, Y. N., and Jan, L. Y. (1998) *Nature* **392,** 775–778
2. Guo, M., Bier, E., Jan, L. Y., and Jan, Y. N. (1995) *Neuron* **14,** 913–925
3. Giesen, K., Hummel, T., Stollewerk, A., Harrison, S., Travers, A., and Klambt, C. (1997) *Development* **124,** 2307–2316
4. Nakamura, M., Okano, H., Blendy, J. A., and Montell, C. (1994) *Neuron* **13,** 1–20
5. Okabe, M., Imai, T., Kurusu, M., Hiromi, Y., and Okano, H. (2001) *Nature* **411,** 94–97
6. Okano, H., Imai, T., and Okabe, M. (2002) *J. Cell Sci.* **115,** 1355–1359
7. Temple, S., and Alvarez-Buylla, A. (1999) *Curr. Opin. Neurobiol.* **9,** 135–141
8. Sakakibara, S., Imai, T., Hamaguchi, K., Okabe, M., Aruga, J., Nakajima, K., Yasutomi, D., Nagata, T., Kurihara, Y., Uesugi, S., Miyata, T., Ogawa, M., Mikoshiba, K., and Okano, H. (1996) *Dev. Biol.* **176,** 230–242
9. Sakakibara, S., and Okano, H. (1997) *J. Neurosci.* **17,** 8300–8312
10. Kaneko, Y., Sakakibara, S., Imai, T., Suzuki, A., Nakamura, Y., Sawamoto, K., Ogawa, Y., Toyama, Y., Miyata, T., and Okano, H. (2000) *Dev. Neurosci.* **22,** 139–153
11. Szabo, A., Dalmau, J., Manley, G., Rosenfeld, M., Wong, E., Henson, J., Posner, J. B., and Furneaux, H. M. (1991) *Cell* **67,** 325–333
12. Liu, J., Dalmau, J., Szabo, A., Rosenfeld, M., Huber, J., and Furneaux, H. (1995) *Neurology* **45,** 544–550
13. Okano, H. J., and Darnell, R. B. (1997) *J. Neurosci.* **17,** 3024–3037
14. Akamatsu, W., Okano, H. J., Osumi, N., Inoue, T., Nakamura, S., Sakakibara, S., Miura, M., Matsuo, N., Darnell, R. B., and Okano, H. (1999) *Proc. Natl. Acad. Sci. U. S. A.* **17,** 9885–9890
15. Sakakibara, S., Nakamura, Y., Yoshida, T., Shibata, S., Koike, M., Takano, H., Ueda, S., Uchiyama, Y., Noda, T., and Okano, H. (2002) *Proc. Natl. Acad. Sci. U. S. A.* **99,** 15194–15199
16. Imai, T., Tokunaga, A., Yoshida, T., Hashimoto, M., Mikoshiba, K., Weinmaster, G., Nakafuku, M., and Okano, H. (2001) *Mol. Cell Biol.* **21,** 3888–3900
17. Kurihara, Y., Nagata, T., Imai, T., Hiwatashi, A., Horiuchi, M., Sakakibara, S., Katahira, M., Okano, H., and Uesugi, S. (1997) *Gene (Amst.)* **186,** 21–27
18. Hodgkin, J., Plasterk, R. H. A., and Waterston, R. H. (1995) *Science* **270,** 410–414
19. Kenan, D. J., Query, C. C., and Keene, J. D. (1991) *Trends Biochem. Sci.* **16,** 214–220
20. Birney, E., Kumar, S., and Krainer, A. R. (1993) *Nucleic Acids Res.* **21,** 5803–5816
21. Burd, C. G., and Dreyfuss, G. (1994) *Science* **265,** 615–621
22. Nagai, K., Oubridge, C., Ito, N., Avis, J., and Evans, P. (1995) *Trends Biochem. Sci.* **20,** 235–240
23. Tsai, D. E., Harper, D. S., and Keene, J. D. (1991) *Nucleic Acids Res.* **19,** 4931–4936
24. Buckanovich, R. J., and Darnell, R. B. (1997) *Mol. Cell Biol.* **17,** 3194–3201
25. Nagata, T., Kanno, R., Kurihara, Y., Uesugi, S., Imai, T., Sakakibara, S., Okano, H., and Katahira, M. (1999) *J. Mol. Biol.* **287,** 315–330
26. Delaglio, F., Grzesiek, S., Vuister, G. W., Zhu, G., Pfeifer, J., and Bax, A. (1995) *J. Biomol. NMR* **6,** 277–293
27. Garrett, D. S., Powers, R., Gronenborn, A. M., and Clore, G. M. (1991) *J. Magn. Reson.* **95,** 214–220
28. Katahira, M., Miyanoiri, Y., Enokizono, Y., Matsuda, G., Nagata, T., Ishikawa, F., and Uesugi, S. (2001) *J. Mol. Biol.* **311,** 973–988
29. Nagata, T., Kurihara, Y., Matsuda, G., Saeki, J., Kohno, T., Yanagida, Y., Ishikawa, F., Uesugi, S., and Katahira, M. (1999) *J. Mol. Biol.* **287,** 221–237
30. Brünger, A. T. (1993) *X-PLOR Version 3.1: A System for X-ray Crystallography and NMR*, Yale University Press, New Haven, CT
31. Laskowski, R. A., Rullmann, J. A., MacArthur, M. W., Kaptein, R., and Thornton, J. M. (1996) *J. Biomol. NMR* **8,** 477–486
32. Nicholls, A., Sharp, K. A., and Honig, B. (1991) *Proteins* **11,** 281–296
33. Lipari, G., and Szabo, A. (1982) *J. Am. Chem. Soc.* **104,** 4546–4559
34. Mandel, A. M., Akke, M., and Palmer, A. G. (1995) *J. Mol. Biol.* **246,** 144–163
35. Clore, G. M., Szabo, A., Bax, A., Kay, L. E., Driscoll, P. C., and Gronenborn, A. M. (1990) *J. Am. Chem. Soc.* **112,** 4989–4991
36. Palmer, A. G., Rance, M., and Wright, P. E. (1991) *J. Am. Chem. Soc.* **113,** 4371–4380
37. Merrill, B. M., Stone, K. L., Cobianch, F., Wilson, S. H., and Williams, K. R. (1988) *J. Biol. Chem.* **263,** 3307–3313
38. Mittermaier, A., Varani, L., Muhandiram, D. R., Kay, L. E., and Varani, G. (1999) *J. Mol. Biol.* **294,** 967–979

Differentiation (2003) 71:486-495

ORIGINAL ARTICLE

Tetsu Yoshida · Akinori Tokunaga · Keiko Nakao · Hideyuki Okano

Distinct expression patterns of splicing isoforms of mNumb in the endocrine lineage of developing pancreas

Received July 9, 2003; accepted in revised form August 21, 2003

Abstract The pancreas is composed of three tissues: endocrine, exocrine, and duct. The endocrine/exocrine lineages diverge from the ductal lineage before E12.5 in mice, and then further separate into endocrine and exocrine precursors. These processes are regulated by differential activation of Notch1-mediated signaling, which is required to repress the expression of the pro-endocrine gene *neurogenin3* (*ngn3*) in the exocrine lineage. Mammalian Numb (mNumb) is an ortholog of *Drosophila* Numb (dNumb), which is likely to be an intracellular inhibitor of Notch signaling, and has four splicing isoforms: PTBS-PRRS, PTBL-PRRS, PTBS-PRRL, and PTBL-PRRL. Here we developed an anti-PRRL antibody, which recognizes only the PRRL forms of mNumb. We then performed immunohistochemical analyses using anti-PRRL together with anti-pan Numb, which recognizes all the isoforms of mNumb, antibodies that determine the spatio-temporal expression pattern of mNumb in the mouse fetal pancreas. mNumb PRRS and PRRL were first expressed in identical cells in the early stage of pancreatic development (i.e., E10.5), but gradually became biased. At the stage of endocrine and exocrine divergence, mNumb PRRS continued to be expressed in endocrine lineage cells, whereas PRRL was down-regulated during endocrine differentiation. Even after the endocrine/exocrine divergence, *notch1* expression was sustained in endocrine lineage, where *ngn3* was expressed. These results agree with the notion that mNumb PRRS has an inhibitory effect on Notch signaling, indicating its potential roles in the differentiation of pancreatic endocrine lineage. In addition, islet cells, which are produced from ductal tissue, were immunostained by the anti-panNb antibody. Our present results will contribute to the understanding of the mechanisms of islet development from ductal tissue.

Key words mNumb · pancreas · Notch signaling · Ngn3 · splicing isoforms

Tetsu Yoshida · Akinori Tokunaga · Keiko Nakao · Hideyuki Okano (✉)
Department of Physiology
Keio University School of Medicine
35 Shinanomachi, Shinjuku-ku
Tokyo 160–8582
Japan
Tel: 81-3-5363-3747, Fax: 81-3-3357-5445
e-mail: hidokano@sc.itc.keio.ac.jp

Akinori Tokunaga · Keiko Nakao · Hideyuki Okano
Core Research for Evolutional Science and Technology (CREST)
Japan Science and Technology Corporation
Saitama 332-0012
Japan

Introduction

The pancreas consists of three types of tissue: endocrine, exocrine, and duct (Slack, 1995). Furthermore, there are four kinds of endocrine cells: glucagon-secreting α-cells, insulin-producing β-cells, somatostatin-expressing δ-cells, and PP-cells, which express pancreatic polypeptide. On the other hand, exocrine cells produce digestive enzymes, such as amylase.

Development of the pancreas begins with evagination of the Pdx1-expressing pancreatic epithelium at around the 15-somite stage in mice (Slack, 1995). From these Pdx1-positive precursor cells, the ductal lineage first diverges between E9.5 and E12.5 and the ductal lineage cells no longer express Pdx1 (Gu et al., 2002). On the other hand, Pdx1-expressing cells form duct-like structures (Guz et al., 1995). By detailed lineage (Gu et al., 2002, 2003) and DNA microarray (Chiang and Melton, 2003) analyses, these Pdx1-positive cells in the duct-like structures were revealed to be common progenitors of both endocrine and exocrine cells.

Notch signaling plays an important role in cell–cell interactions to determine the cell fate not only of the pancreas but also of various other organs, and this function is conserved from invertebrates to vertebrates (Artavanis-Tsakonas et al., 1999). Notch signaling plays an important role in the divergence of the exocrine/endocrine lineages from the Pdx1-positive cells in the duct-like structures (Apelqvist et al., 1999; Jensen et al., 2000b). Previous reports indicate that Notch signaling-activated cells differentiate into exocrine cells, while Notch signaling-inhibited cells become endocrine cells (Apelqvist et al., 1999; Gradwohl et al., 2000; Jensen et al., 2000a; Schwitzgebel et al., 2000).

mNumb is a factor that modulates Notch signaling; it is an adaptor molecule with a phosphotyrosine-binding (PTB) domain, which binds to the Notch intracellular domain, and a proline-rich region (PRR), which binds to the SH3 domain of other proteins (Zhong et al., 1996). Three E3 ubiquitin ligase proteins, LNX (Nie et al., 2002), Mdm2 (Juven-Gershon et al., 1998), and Siah-1 (Susini et al., 2001), also physically interact with mNumb, indicating that these proteins can be recruited by mNumb to degrade Notch protein and thus inhibit Notch signaling.

Drosophila Numb (Uemura et al., 1989), an ortholog of mNumb, functions antagonistically to Notch signaling by interacting both with the ankyrin repeat of Notch and with adaptin, which directs Notch to the endocytosis complex, where Notch is degraded (Guo et al., 1996; Berdnik et al., 2002). By analogy to *Drosophila* Numb, mNumb was initially thought to modulate Notch signaling negatively through direct protein–protein interaction with the ankyrin repeat of Notch1 (Sestan et al., 1999; Wakamatsu et al., 1999). However, recent studies have shown that the role of mNumb is not as simple as first believed. mNumb knock-out (KO) mice, for example, show a similar phenotype to that of Notch1/Notch4 double KO mice (Krebs et al., 2000; Zilian et al., 2001). Moreover, a decreasing number of mitotic cells and an increasing number of differentiating cells were observed in the nervous system of *numb* and *numblike* double KO mice at around E10 (Petersen et al., 2002).

Recent studies show that mNumb has two splicing variant sites in its PTB domain and PRR that give rise to four splicing isoforms, PTBL-PRRL, PTBL-PRRS, PTBS-PRRL, and PTBS-PRRS (Dho et al., 1999; Verdi et al., 1999). Functional differences between PTBL and PTBS have not been determined, although their differential intracellular localization has been reported: PTBL localizes to the plasma membrane, while PTBS localizes to the cytoplasm (Dho et al., 1999). On the other hand, some potential functional differences between PRRL and PRRS have been identified (Verdi et al., 1999). While mNumb PRRS isoforms cause cell cycle arrest and initiate differentiation, mNumb PRRL isoforms have been shown to promote cell proliferation in culture.

To gain further insight into the functions of the distinct mNumb PRR isoforms *in vivo*, we developed a specific antibody to mNumb PRRL (designated the anti-PRRL antibody), which reacts with the PRRL splicing isoforms, as well as an anti-pan Numb antibody that recognizes all the splicing isoforms of mNumb. In this report, focusing on pancreatic development, we used these antibodies to analyze the spatio-temporal expression pattern of distinct isoforms of mNumb by immunohistochemical analyses. All of the splicing isoforms of mNumb were expressed in the early pancreas, although mNumb PRRL showed biased expression in exocrine cells at E14.5. mNumb was also expressed in islets that were differentiated from ductal tissue. These results suggest that mNumb PRRS and PRRL play different roles in endocrine differentiation.

Methods

Antibodies

Numb-specific antisera were generated in rabbits immunized with peptides corresponding to different regions of Numb conjugated to KLH as follows: anti-pan Numb (panNb), CTTHPHQSPSLAKQQTFPQYE; anti-PRRL, CMPVRETNP-WAHVPDAANKE. The crude serum was affinity purified using synthetic peptides of the corresponding regions of mNumb. Mouse anti-insulin (I2018) and anti-glucagon (G2654) antibodies were obtained from Sigma-Aldrich (St. Louis, MO). Goat anti-amylase (C-20, SC-12821; Santa Cruz Biotechnology, Inc., Santa Cruz, CA), rabbit anti-Numb (07-147; Upstate Biotechnology, Lake Placid, NY), rabbit anti-Glut2 (AB1342; Chemicon, Temecula, CA), mouse anti-CK19 (11417; ICN Biochemicals, Inc., Aurora, OH), and guinea pig anti-insulin C peptide (1021-K, Linco Research, Inc., St. Charles, MO) antibodies were also used.

Recombinant plasmids

cDNAs of mNumb PTBS-PRRS, PTBS-PRRL, and Numblike were obtained from a mouse embryo cDNA library by PCR, and were sub-cloned into the mammalian expression vector pcDNA3 (Invitrogen, Carlsbad, CA). To obtain fusion proteins of EGFP-mNumb PTBS-PRRS, -mNumb PTBS-PRRL, and -Numblike, cDNAs were also sub-cloned into the pEGFP-C1 vector (Stratagene, La Jolla, CA).

Immunoblot analysis

Twenty micrograms of protein were loaded in each lane and separated by 7.5% SDS-PAGE. Proteins were transferred to an Immobilon transfer membrane (Millipore, Bedford, MA) and probed with the anti-pan Numb or anti-PRRL antibody. The chemiluminescent signals were detected by ECL (Amersham Pharmacia Biotechnologies, Piscataway, NJ) with Kodak X-OMAT film (Kodak, Rochester, NY), according to the manufacturer's instructions.

Animals and tissue preparation

C57BL/6 mice, used for the preparation of tissue protein extracts or tissue sections, were obtained from Charles River Japan, Inc. (Kanagawa, Japan). The date of conception was established by the presence of a vaginal plug and recorded as E0.5.

In situ hybridization and immunohistochemistry

In *situ* hybridization and immunohistochemistry were performed as described elsewhere (Jensen et al., 2000a; Chiang and Melton, 2003).

Optical sections were viewed using a scanning laser confocal imaging system (Zeiss LSM510). Images were processed using Adobe Photoshop 6.0 (Adobe Systems). Bright field and Nomarski imaging were performed using a Zeiss Axioplans2 microscope.

Results

Development and specificity of antibodies recognizing mNumb

To examine the immunolocalization of mNumb PRRS and PRRL, we developed an anti-PRRL antibody that recognizes the PRRL splicing isoforms of mNumb, and an anti-pan Numb (panNb) antibody that recognizes all the splicing isoforms of mNumb (Fig. 1A). We then determined the specificity of the antibodies by testing their ability to specifically recognize ectopically expressed mNumb proteins. Two proteins, mNumb PRRS (NbPRRS) and mNumb PRRL (NbPRRL), expressed in Cos7 cells were analyzed by immunoblot analysis using the anti-panNb and anti-PRRL antibodies (Fig. 1B, left two panels). This analysis confirmed that the anti-panNb antibody recognized both mNumb PRRS and PRRL, while the anti-PRRL

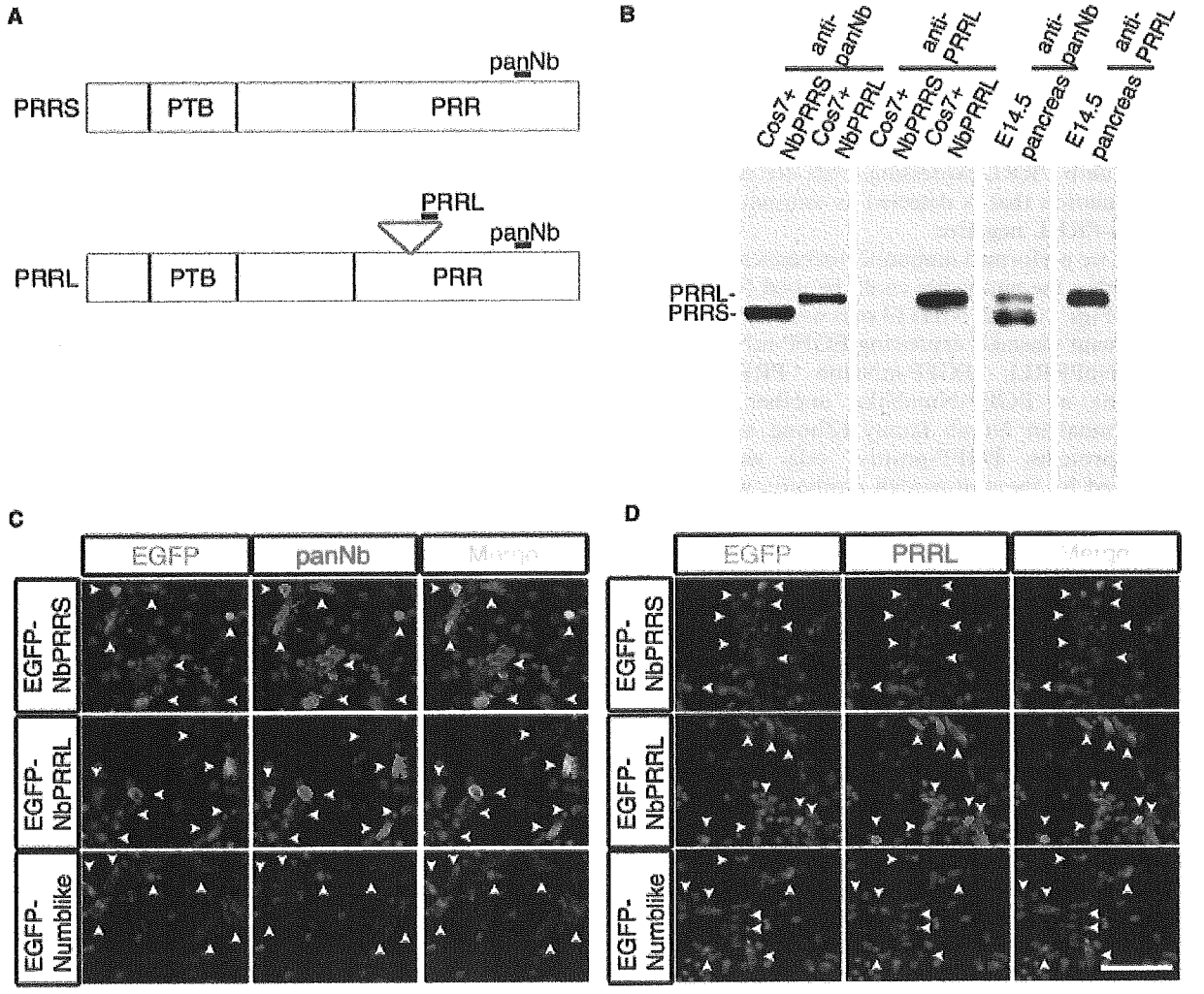

Fig. 1 Splicing isoforms of mNumb and the specificity of anti-panNb and anti-PRRL antibodies. (**A**) Schematic representation of the mNumb isoforms with different splicing in the PRR (proline-rich region): short form (PRRS) and long form (PRRL). The recognition sites of the anti-PRRL and anti-pan Numb (panNb) antibodies are also indicated above the schemes. (**B**) Immunoblot analysis using anti-panNb and anti-PRRL antibodies. Left two panels: mNumb PRRS and PRRL proteins were transiently expressed in Cos7 cells, and the cell lysates were analyzed by immunoblotting with the indicated antibodies. Right two panels: E14.5 mouse pancreata were dissected and lysed by SDS sample buffer. Immunoblot analyses were performed with the indicated antibodies. (**C**, **D**) EGFP-mNumb PRRS (EGFP-NbPRRS), EGFP-mNumb PRRL (EGFP-NbPRRL), and EGFP-Numblike fusion proteins were independently expressed in NIH3T3 cells. The cells were immunostained with anti-panNb (C, red) or anti-PRRL (D, red) antibodies followed by observation of the EGFP fluorescence (arrowheads). Nuclei of the cells were counterstained by Hoechst (blue). The scale bar represents 50 μm.

antibody only recognized mNumb PRRL. In addition, an immunoblot analysis of E14.5 mouse pancreas lysate with anti-panNb and anti-PRRL antibodies showed only two and one bands, respectively, the sizes of which corresponded to the ectopically expressed proteins in Cos7 cells (Fig. 1B, right two panels). Immunoblot analysis of pancreas lysates prepared at different stages showed that the levels of these proteins stayed almost the same throughout pancreatic development (data not shown). Thus, mNumb PRRL-expressing, but not mNumb PRRS-expressing, cells could be identified as anti-panNb and anti-PRRL double-positive cells. However, it should be noted that, if mNumb PRRS and mNumb PRRL are co-localized in the same cells, these cells are detected as anti-panNb and anti-PRRL double positive. Thus, it is possible that cells expressing both mNumb PRRS and PRRL are included among the cells detected also as anti-panNb anti-PRRL double-positive cells. On the other hand, mNumb PRRS-expressing, but not mNumb PRRL-expressing, cells are recognized as the population that is detected as anti-panNb positive and anti-PRRL negative.

Next, we performed immunocytochemical analyses to test whether the antibodies could be used for immunostaining (Figs. 1C,1D). NIH3T3 cells were transfected with recombinant plasmids expressing EGFP-mNumb PRRL (EGFP-NbPRRL), EGFP-mNumb PRRS (EGFP-NbPRRS), or EGFP-Numblike, another member of the mammalian Numb family (Zhong et al., 1997), fusion proteins. EGFP-positive cells were strongly recognized by the anti-panNb antibody, while EGFP-Numblike-positive cells were not (Fig. 1C). On the other hand, the anti-PRRL antibody recognized only the cells containing the EGFP-NbPRRL fusion protein (Fig. 1D). These results showed that the two antibodies, anti-panNb and anti-PRRL, recognized the correct epitopes and did not recognize other proteins. We compared the specificity of the anti-panNb antibody we made to that of a commercially available anti-Numb antibody that was developed against the identical peptide we used for developing the anti-panNb antibody and is commercially sold (Cayouette and Raff, 2003), by immunohistochemical analysis of an E18.5 pancreas and found that both showed almost the same results (data not shown). In addition, immunoprecipitation analyses confirmed the specificity of the anti-PRRL antibody. Proteins precipitated with the anti-panNb antibody from mouse brain lysate were recognized by the anti-PRRL antibody, and proteins precipitated with the anti-PRRL antibody were also recognized by the anti-panNb antibody (data not shown).

Expression pattern of mNumb in the early developing pancreas

We next performed immunohistochemistry to observe the expression pattern of mNumb in the developing pancreas. First, the expression pattern of mNumb was compared with that of *pdx1* as an early pancreatic cell marker (Fig. 2). We performed *in situ* hybridization to detect the mRNA of *pdx1*, followed by immunostaining with the anti-panNb antibody (Figs. 2A,2B). mNumb was expressed in many cells of the whole body as described previously (Zhong et al., 1997), and we found

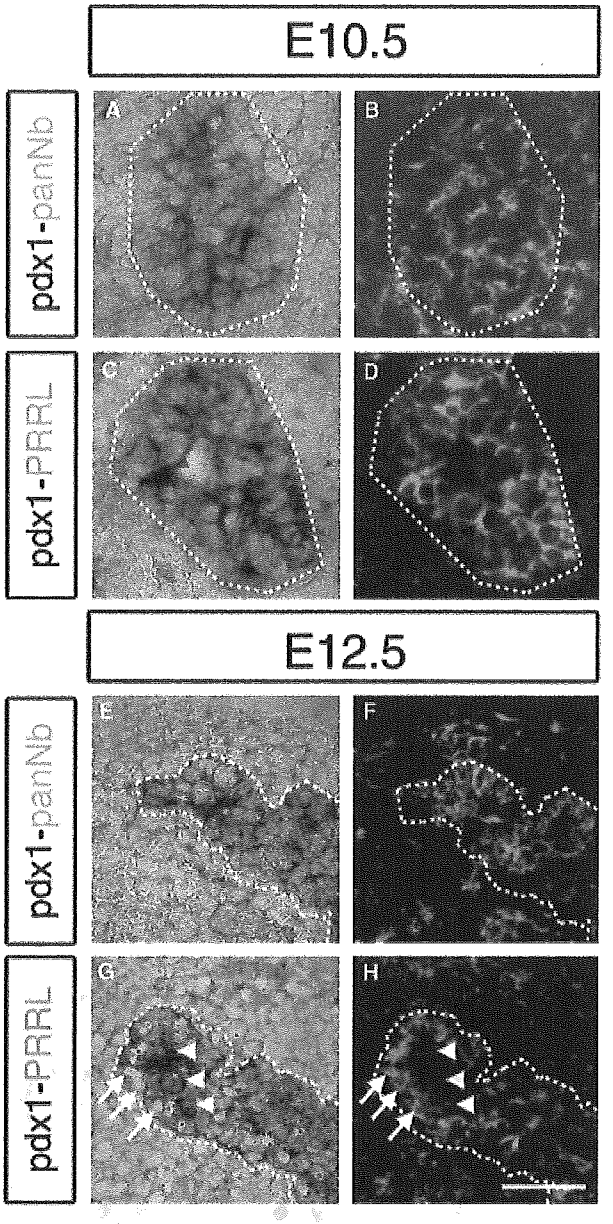

Fig. 2 mNumb is expressed in *pdx1*-positive cells of the early developing pancreas. *In situ* hybridization of *pdx1* mRNA was performed (**A**, **C**, **E**, **G**) followed by immunostaining using anti-panNb (**B**, **F**, green) and anti-PRRL (**D**, **H**, green) antibodies in E10.5 (A–D) and E12.5 (E–H) mouse embryos. *pdx1*-positive cells are surrounded by dotted lines. *pdx1* strong-positive cells and weak-positive cells in (G) and (H) are indicated by arrows and arrowheads, respectively. The scale bar represents 50 μm.

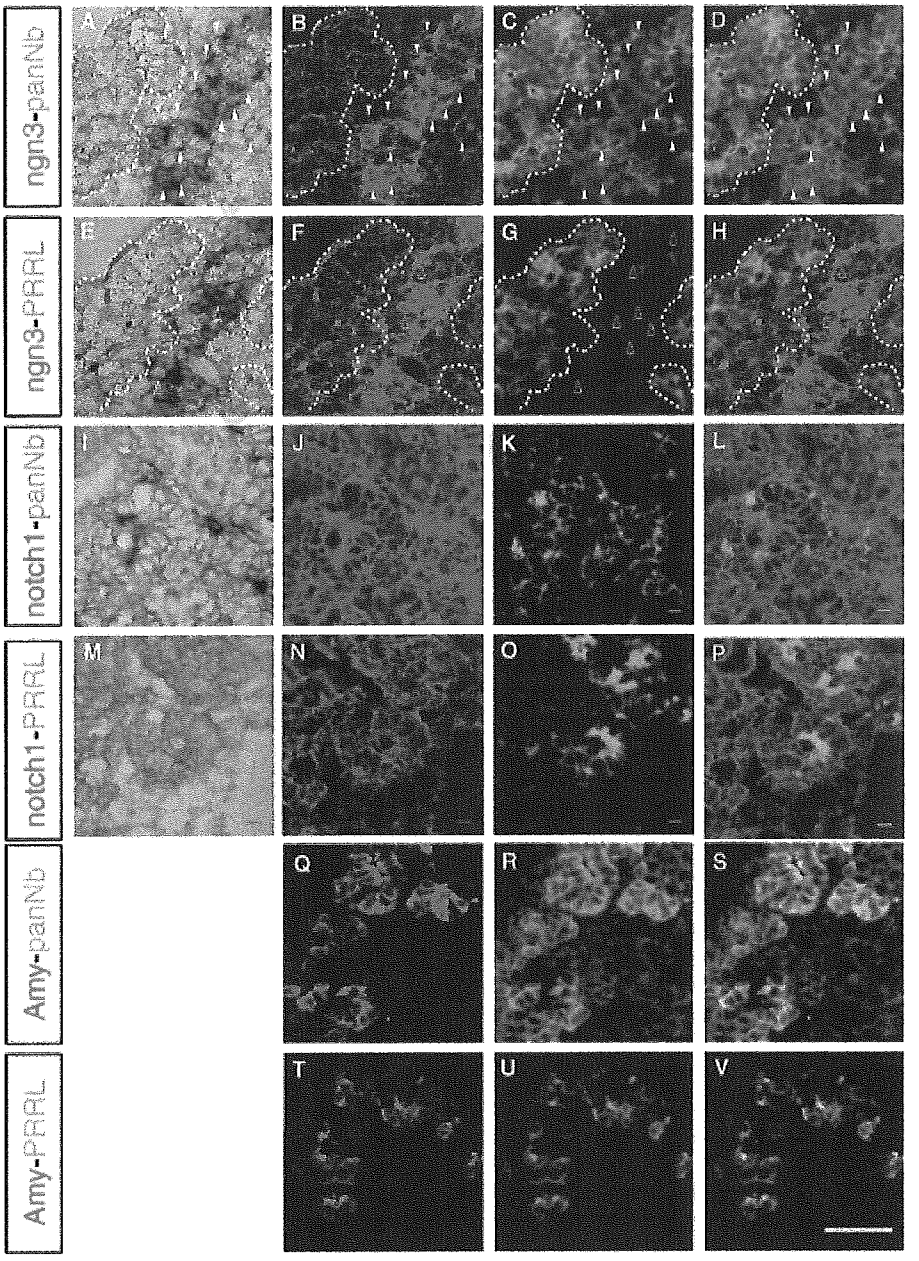

Fig. 3 mNumb, but not mNumb PRRL, is expressed in *ngn3*-positive cells of the E14.5 mouse pancreas. *In situ* hybridization of *ngn3* (A, E) and *notch1* (I, M) mRNA was performed, followed by immunostaining using anti-panNb (C, K, green) and anti-PRRL (G, O, green) antibodies in an E14.5 mouse embryo. (B F, J, N) The pseudo-color (red) of the *in situ* hybridization signals under Nomarski imaging. (**A–D**) *ngn3* mRNA-positive and anti-panNb antibody immunoreactive cells are marked by solid arrowheads. *ngn3* mRNA-negative and anti-panNb immunoreactive cells are surrounded by dotted lines. (**E–H**) *ngn3* mRNA-positive and anti-PRRL antibody-negative cells are marked by open arrowheads. (**I–L**) *notch1* mRNA-positive cells in duct-like structures are detected by anti-panNb antibody. (**M–P**) *notch1* mRNA is also detected in anti-PRRL antibody-recognizing cells. (**Q–V**) *ngn3* mRNA-negative and anti-panNb or anti-PRRL immunoreactive cells (surrounded by dotted lines in A–H) are exocrine cells. (Q–S) Double immunostaining using anti-amylase (Amy; Q, red) and anti-panNb (R, green) antibodies. (T–V) Double immunostaining using anti-amylase (T, red) and anti-PRRL (U, green) antibodies. (D, H, L, P, S, V) Merged images. The scale bar represents 50 μm.

that the strongest anti-panNb immunostaining was observed in the *pdx1*-expressing pancreatic bud cells. Immunostaining with the anti-PRRL antibody was also examined, and the expression of mNumb PRRL was also detected in the pancreatic bud (Figs. 2C,2D). At E12.5, *pdx1*-expressing cells are localized to portions of the cell population called duct-like structures (Figs. 2E–2H, dotted lines; Guz et al., 1995; Jensen et al., 2000a; Gu et al., 2002). *In situ* hybridization analysis revealed that although some of these cells strongly expressed *pdx1*, others did so only weakly. We assume that *pdx1* weak positive cells may be the progenitors of exocrine cells, in which the expression of Pdx1 has been shown to decrease gradually (Guz et al., 1995). Although immunohistochemistry with the anti-panNb antibody revealed that mNumb was strongly expressed in the *pdx1*-positive cells, mNumb was also weakly expressed in *pdx1*-negative cells in the pancreatic anlagen (Figs. 2E,2H). However, mNumb PRRL was only weakly expressed in *pdx1* strong positive cells (Figs. 2G,2H, arrowheads), and strongly detected in *pdx1* weak positive cells (arrows). Collectively, the expression levels of mNumb PRRL and *pdx1* appeared to be negatively correlated within the duct-like structures.

At E14.5, the bHLH gene *ngn3* begins to be expressed in the *pdx1*-positive duct-like structure cells from which

endocrine cells are differentiated (Gradwohl et al., 2000; Jensen et al., 2000a; Schwitzgebel et al., 2000; Gu et al., 2002). It has been shown that the exocrine acinar cells, which express digestive enzymes such as amylase, also originate from the duct-like structures (Apelqvist et al., 1999; Jensen et al., 2000b). The signal detected by the anti-panNb antibody virtually overlapped with that of *ngn3* detected by *in situ* hybridization (Figs. 3A–3D, solid arrowheads) in the duct-like structures. The anti-panNb signal was also detected in the *ngn3*-negative cells (Figs. 3A–3D, dotted line), which in turn expressed amylase, meaning they were exocrine cells (Figs. 3Q–3S). On the other hand, because the immunoreactivity of the anti-PRRL antibody was not observed in the duct-like structures, the expression of *ngn3* and mNumb PRRL did not overlap (Figs. 3E–3H, open arrowheads). The anti-PRRL immunoreactivity completely overlapped with amylase (Figs. 3T–3V).

In addition, the relationship between the expression of *notch1* and mNumb was examined. *notch1* mRNA has been reported to be expressed in almost all of the pancreatic cells, including duct-like structures and acinar cells at E14.5 (Lammert et al., 2000), though the expression remains only in exocrine cells at E17.5 (Jensen et al., 2000a). In the present study, we found that cells expressing *notch1* mRNA co-express both mNumb PRRS and *ngn3* mRNA in duct-like structures (Figs. 3I–3L) at E14.5. At the same stage, the double staining by *in situ* hybridization of *notch1* and immunohistochemistry using anti-PRRL antibody revealed that *notch1* and mNumb PRRL also co-expressed in exocrine cells (Figs. 3M–3P). Collectively, expression of mNumb PRRL disappeared in endocrine lineage cells, which expressed *notch1*, mNumb PRRS, and *ngn3*, whereas expression of mNumb PRRL continued in exocrine lineage cells, in which *ngn3* was not expressed.

Expression of mNumb in the perinatal pancreas

Because mNumb PRRS was expressed in the *ngn3*-positive cells at E14.5, we next examined the expression of mNumb isoforms in various cell types that emerge within the islet at E18.5. The endocrine cells form a cluster designated as an islet, which is a cluster of insulin-producing β-cells surrounded by one cell layer of α-cells, which produce glucagon (Figs. 4A–4C). The signals of the anti-panNb and anti-insulin antibodies almost completely overlapped each other (Figs. 4D–4F), while the expressions of mNumb and glucagon were complementary (Figs. 4G–4I).

During pancreatic development, the dorsal pancreatic bud (corresponding to the "tail" of the pancreas in adults) and ventral pancreatic bud (corresponding to the "head" of the pancreas) fuse (reviewed by Slack, 1995). The ventral duct also fuses with the distal part of the dorsal duct to become the main pancreatic duct

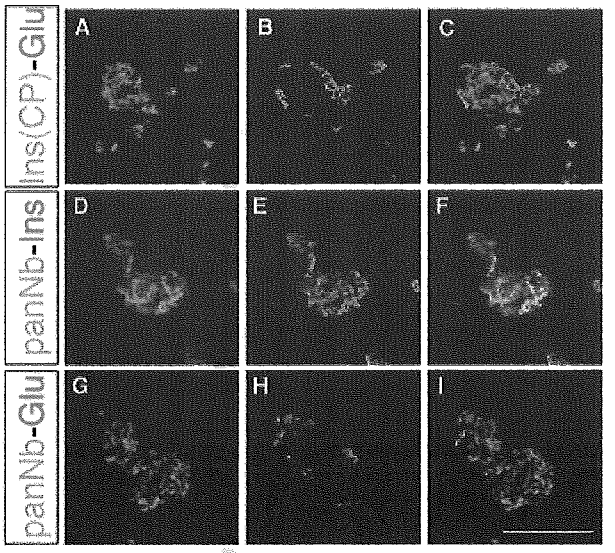

Fig. 4 mNumb is expressed in β-cells, but not α-cells, in the perinatal mouse pancreas. (**A–C**) Double immunostaining using anti-insulin C peptide (Ins[CP]; A, green) and anti-glucagon (Glu; B, red) antibodies. (**D–F**) Double immunostaining using anti-panNb (D, green) and anti-insulin (Ins; F, red) antibodies. Essentially all the insulin-positive β-cells are immunostained with anti-panNb antibody. (**G–I**) Double immunostaining using anti-panNb (G, green) and anti-glucagon (I, red) antibodies. Note that the expression patterns of mNumb and glucagon are complementary. (C, F, I) Merged images. The scale bar represents 100 μm.

(duct of Wirsung; Figs. 5A,5B). The proximal part of the dorsal duct becomes a small accessory duct (duct of Santorini). Many data suggest that the islets originate from the tissue around these main ducts, from the perinatal stage to 2 weeks after birth (reviewed in Swenne, 1992). Thus, we observed mNumb expression in ductal tissue, whether or not mNumb is expressed in new islets generated from ductal tissue as was the case in new islets generated from duct-like structures.

There were many anti-panNb-positive cell clusters (Fig. 5D, arrows and arrowheads), the size of which was similar to that of islets (Fig. 5C), around the duct (asterisks). The anti-panNb-positive cell clusters were classified into two groups based on the immunostaining of successive sections with various markers (Figs. 5F,5H,5J,5L). Specificity of the immunostainings was confirmed by the visual identification of islets in identical sections (Figs. 5E,5G,5I,5K). Based on these results, the cell clusters in the ductal tissue were classified into CK19-positive (Fig. 5F, arrow) and CK19-negative (Fig. 5F, arrowheads) groups.

CK19 is known to be a marker molecule of pancreatic duct cells, and CK19-positive cell clusters budding from main ducts have been shown to be progenitors of islets (Bouwens et al., 1994). Little expression of mNumb was detected in these cells, which also did not express insulin, glucagon, or Glut2 (Fig. 5, arrows). On the other hand, weak expression of

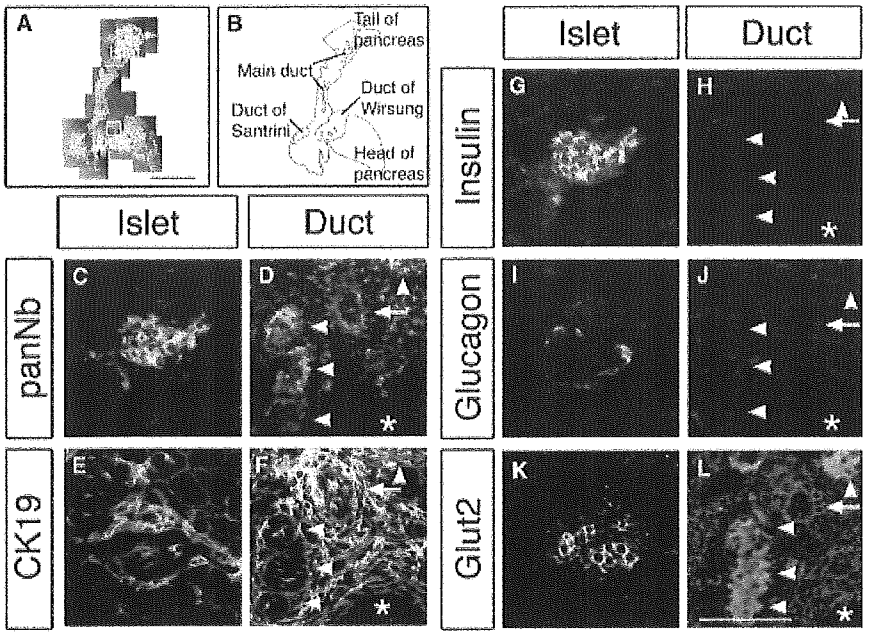

Fig. 5. New islets generated from the duct also express mNumb. **(A)** An E18.5 mouse pancreas in bright field was observed under low magnification. The positions of the islets and duct cells shown in (C)–(L) are indicated. **(B)** Delineation of the E18.5 pancreas shown in (A). The positions of the main ducts, the duct of Santrini and duct of Wirsung, are indicated. **(C–L)** Serial sections of an E18.5 pancreas were immunostained by anti-panNb (C, D), anti-CK19 (E, F), anti-insulin (G, H), anti-glucagon (I, J), and anti-Glut2 (K, L) antibodies. Islets and tissue around the duct of Wirsung (Duct) were observed in identical sections. Asterisks indicate duct holes. Arrows indicate budding cell clusters from the duct hole. Arrowheads indicate insulin-negative, glucagon-negative, but Glut2-positive cell clusters, suggesting that they are the precursors of endocrine cells. The scale bars represent 1 mm (A) and 100 μm (C–L).

mNumb was detected in CK19-negative cell clusters, which were insulin- and glucagon-negative but Glut2-positive cells (Fig. 5, arrowheads). Although Glut2 is the functional molecule that is expressed in β-cells, it is reported that many insulin-negative but Glut2-positive cells are observed, which are likely to be progenitors of insulin- and Glut2-positive β-cells (Pang et al., 1994).

Collectively, mNumb was expressed in immature islets, which are differentiated from ductal tissue, and in mature β-cells, suggesting that mNumb is involved in the differentiation of β-cells from duct cells.

Discussion

Expression of mNumb PRRS and PRRL is different among cell types in the embryonic pancreas

Our understanding of the function of Numb has mainly come from analysis of the differentiation of the *Drosophila* peripheral nervous system, which is made up of four cells originating from one cell called the sensory organ precursor (SOP) cell (reviewed by Lu et al., 2000). When the SOP cell divides, Numb protein is inherited by only one of the daughter cells (the IIb cell), in which Notch signaling is inhibited, whereas Notch signaling is activated in the other cell (the IIa cell). As a result, the two daughter cells give rise to different lineages. This mechanism in which Numb influences cell type determination is preserved in various aspects of neuronal differentiation in vertebrates, such as in the chick dorsal root ganglia (Wakamatsu et al., 1999) and the mouse retina (Cayouette and Raff, 2003).

It is reported that cell cycle arrest occurs and differentiation begins when mNumb PRRS is expressed (Zhong et al., 1996). Although mNumb PRRL is known to direct cell proliferation (Verdi et al., 1999), its underlying mechanisms as well as its *in vivo* function are not clear. In this report, we used two antibodies to discriminate distinct splicing isoforms of mNumb and analyzed their spatio-temporal expression by immunohistochemical methods. Our results showed that different splicing isoforms in the proline-rich region of mNumb (mNumb PRRS and mNumb PRRL) have different expression patterns in endocrine differentiation, raising the possibility that they have different functions.

Immunoblot analysis showed that both the PRRL and PRRS isoforms of mNumb are expressed at an almost comparable level throughout pancreatic development (data not shown). Immunohistochemical analyses demonstrated that mNumb PRRL was expressed in almost all the *pdx1*-expressing cells in the early developing pancreas (Figs. 2C,2D). While mNumb PRRL was still expressed in the *pdx1*-positive duct-like structures in the E12.5 pancreas, mNumb PRRL was strongly detected in the cells that showed relatively weak *pdx1* expression by *in situ* hybridization (Figs. 2G,2H, arrowheads). It has been reported that Pdx1 is expressed in exocrine cells by E14.5, although the expression detected by an anti-Pdx1 antibody gradually disappears by P0 (Guz et al., 1995). The mNumb PRRL-expressing cells co-expressed a marker of exocrine cells, amylase, at E14.5 (Figs. 4L–4N). These results suggest that mNumb PRRL could be involved in exocrine cell differentiation, and that the mRNA level of *pdx1* decreased by E12.5 in exocrine lineage cells. On

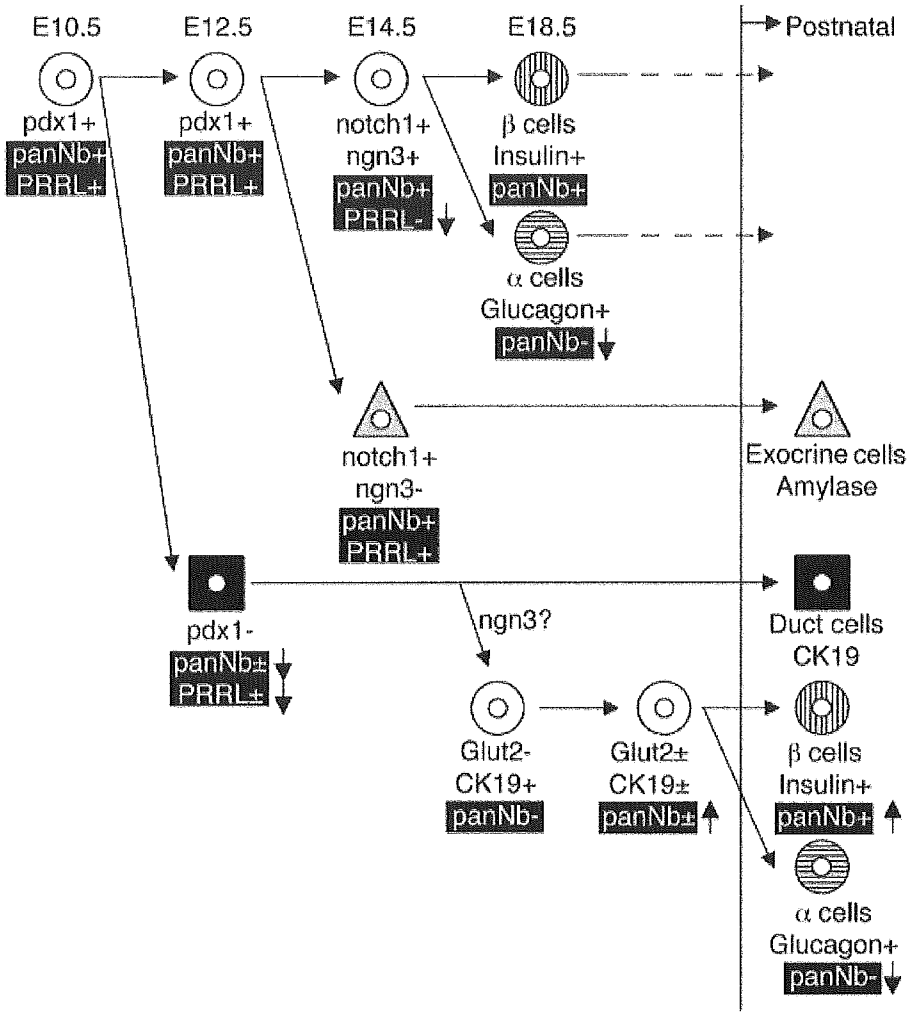

Fig. 6. Schematic representation of the expression pattern of mNumb. *pdx1*-expressing early pancreatic cells were anti-panNb and anti-PRRL double positive. However, the expression of mNumb disappeared in duct cell lineage cells, which are known to diverge first in the E12.5 mouse pancreas. At E14.5, *notch1* is expressed in both *ngn3*-positive endocrine and *ngn3*-negative exocrine lineage cells. In endocrine progenitors, only the expression of mNumb PRRL disappeared, and expression of *notch1* also disappeared at E18.5, though the expression remained in exocrine cells (data not shown; Jensen et al., 2000a). In mature islets, mNumb was detected only in β-cells, and not in α-cells. The expression of mNumb was also observed in the immature islets generated from ductal tissue. See text for details.

the other hand, cells expressing only mNumb PRRS, the anti-panNb-positive but anti-PRRL-negative cells, were observed in the duct-like structures, which are endocrine cell progenitors that transiently express *ngn3* (Figs. 3A–3H; Jensen et al., 2000a; Schwitzgebel et al., 2000; Gu et al., 2002). These results suggest that mNumb PRRS and PRRL might play important roles in the divergence of the endocrine and exocrine cell lineages.

The reasons why Notch signaling is involved in the divergence of the exocrine and endocrine lineages in the pancreas have been discussed (Edlund, 2001); one is to restrict the increasing number of endocrine cells, and another is to promote an increasing number of exocrine cells. Ngn3-expressing endocrine progenitor cells activate the Notch signaling of neighboring cells, thereby inhibiting the expression of Ngn3 in those cells and consequently their differentiation into endocrine cells. Furthermore, the cells in which Notch signaling is activated remain as undifferentiated progenitor cells, which can undergo subsequent proliferation. Actually, *ngn3* and mNumb PRRS were co-expressed in duct-like structure cells, where *notch1* continued to be also expressed (Figs. 3A–3D,3I,3J). It is likely that mNumb PRRS inhibits Notch1 signaling, because previous studies showed that chicken Numb (PRRS) blocked the nuclear translocation of activated chicken Notch1 through direct binding to the PEST sequence in the cytoplasmic domain of chicken Notch1 as well as chicken Notch1-mediated inhibition of neuronal differentiation (Wakamatsu et al., 1999; Y. Wakamatsu, personal communication). These results strongly suggest that mNumb PRRS inhibits Notch signaling in these cells. In addition, mNumb PRRL was expressed in acinar cells (Figs. 3T–3V), suggesting that mNumb PRRL is involved in proliferation of exocrine cells.

Islet synthesis in ductal tissue from the perinatal stage

Several lines of evidence suggest that insulin-producing β-cells are generated from cells existing in pancreatic ductules. It is generally believed that during fetal and

neonatal life, islets are newly formed from clusters of precursor cells that bud off from pancreatic ductules (reviewed in Swenne, 1992). These consist of CK19- and CK20-positive cell clusters, which have been suggested to differentiate into α-cells and β-cells, by bromodeoxyuridine (BrdU) pulse labeling experiments (Bouwens et al., 1994).

The pathway generating new islets from the ducts in postnatal mice may be different from that in the embryonic duct-like structures, because the duct and exocrine/endocrine lineages diverge between E9.5 and E12.5 (Gu et al., 2002). However, endocrine cell differentiation from the duct-like structures in the embryo is largely similar to that from the ductal tissue in postnatal mice. Misexpression of Ngn3 in primary cultures of ductal cells from adult mice results in NeuroD/β2, Pax4, Nkx2.2, Nkx6.1, Pax6, and insulin expression (Bonner-Weir et al., 2000; Heimberg et al., 2000; Heremans et al., 2002). This gene expression cascade induced by the misexpression of Ngn3 is the same as that observed in differentiating endocrine cells in the embryo (Jensen et al., 2000a). It is possible that a minor population of mature pancreatic duct cells activates Ngn3 expression and quickly exits the ducts to form islets (Fig. 6; Gu et al., 2002). Although *ngn3* expression was not detected by *in situ* hybridization (data not shown), endocrine cell marker-negative, Glut2-positive endocrine progenitor cell clusters budding from the main duct were observed (Fig. 5). A stronger expression level of mNumb was observed in progenitor cell clusters that were located away from the duct, while the expression of CK19 became weaker in these cells, and vice versa (Fig. 6). These findings suggest that mNumb may play an important role in islet production from the duct, as it does in endocrine cell differentiation from the duct-like structures in the embryonic stage.

The present study revealed different expression patterns of mNumb PRRS and PRRL in endocrine differentiation. Further studies on the interaction between Notch and mNumb PRRL, the mechanisms of endocrine cell differentiation from ductal tissue, and the mechanisms of endocrine cell type determination after Ngn3 expression will increase our understanding of the roles of the different splicing isoforms of mNumb in endocrine differentiation. mNumb may play roles in the specification of endocrine cells, given that it is selectively expressed in the β-cell lineage and not in the α-cell lineage (Figs. 4D–4I), which would be unequivocally clarified in further studies using conditional knock-out methods.

Acknowledgements We are grateful to Dr. Shin-ichi Sakakibara (Dokkyo University) for his critical reading of the manuscript. We also thank Dr. Yoshio Wakamatsu (Tohoku University) for valuable suggestions. This work was supported by grants to H.O. from the Japanese Ministry of Education, Science, Culture, Sports, and Technology, from CREST, Japan and Technology Corporation, and from the Human Frontier Science Program.

References

Apelqvist, A., Li, H., Sommer, L., Beatus, P., Anderson, D.J., Honjo, T., Hrabe de Angelis, M., Lendahl, U. and Edlund, H. (1999) Notch signalling controls pancreatic cell differentiation. Nature 400:877–881.

Artavanis-Tsakonas, S., Rand, M.D. and Lake, R.J. (1999) Notch signaling: cell fate control and signal integration in development. Science 284:770–776.

Berdnik, D., Torok, T., Gonzalez-Gaitan, M. and Knoblich, J.A. (2002) The endocytic protein α-Adaptin is required for numb-mediated asymmetric cell division in *Drosophila*. Dev Cell 3: 221–231.

Bonner-Weir, S., Taneja, M., Weir, G.C., Tatarkiewicz, K., Song, K.H., Sharma, A. and O'Neil, J.J. (2000) In vitro cultivation of human islets from expanded ductal tissue. Proc Natl Acad Sci USA 97:7999–8004.

Bouwens, L., Wang, R.N., De Blay, E., Pipeleers, D.G. and Kloppel, G. (1994) Cytokeratins as markers of ductal cell differentiation and islet neogenesis in the neonatal rat pancreas. Diabetes 43:1279–1283.

Cayouette, M. and Raff, M. (2003) The orientation of cell division influences cell-fate choice in the developing mammalian retina. Development 130:2329–2339.

Chiang, M.K. and Melton, D.A. (2003) Single-cell transcript analysis of pancreas development. Dev Cell 4:383–393.

Dho, S.E., French, M.B., Woods, S.A. and McGlade, C.J. (1999) Characterization of four mammalian numb protein isoforms. Identification of cytoplasmic and membrane-associated variants of the phosphotyrosine binding domain. J Biol Chem 274:33097–33104.

Edlund, H. (2001) Factors controlling pancreatic cell differentiation and function. Diabetologia 44:1071–1079.

Gradwohl, G., Dierich, A., LeMeur, M. and Guillemot, F. (2000) neurogenin3 is required for the development of the four endocrine cell lineages of the pancreas. Proc Natl Acad Sci USA 97:1607–1611.

Gu, G., Dubauskaite, J. and Melton, D.A. (2002) Direct evidence for the pancreatic lineage: NGN3+ cells are islet progenitors and are distinct from duct progenitors. Development 129:2447–2457.

Gu, G., Brown, J.R. and Melton, D.A. (2003) Direct lineage tracing reveals the ontogeny of pancreatic cell fates during mouse embryogenesis. Mech Dev 120:35–43.

Guo, M., Jan, L.Y. and Jan, Y.N. (1996) Control of daughter cell fates during asymmetric division: interaction of Numb and Notch. Neuron 17:27–41.

Guz, Y., Montminy, M.R., Stein, R., Leonard, J., Gamer, L.W., Wright, C.V. and Teitelman, G. (1995) Expression of murine STF-1, a putative insulin gene transcription factor, in β cells of pancreas, duodenal epithelium and pancreatic exocrine and endocrine progenitors during ontogeny. Development 121:11–18.

Heimberg, H., Bouwens, L., Heremans, Y., Van De Casteele, M., Lefebvre, V. and Pipeleers, D. (2000) Adult human pancreatic duct and islet cells exhibit similarities in expression and differences in phosphorylation and complex formation of the homeodomain protein Ipf-1. Diabetes 49:571–579.

Heremans, Y., Van De Casteele, M., In't Veld, P., Gradwohl, G., Serup, P., Madsen, O., Pipeleers, D. and Heimberg, H. (2002) Recapitulation of embryonic neuroendocrine differentiation in adult human pancreatic duct cells expressing neurogenin 3. J Cell Biol 159:303–312.

Jensen, J., Heller, R.S., Funder-Nielsen, T., Pedersen, E.E., Lindsell, C., Weinmaster, G., Madsen, O.D. and Serup, P. (2000a) Independent development of pancreatic α- and β-cells from neurogenin3-expressing precursors: a role for the notch pathway in repression of premature differentiation. Diabetes 49:163–176.

Jensen, J., Pedersen, E.E., Galante, P., Hald, J., Heller, R.S., Ishibashi, M., Kageyama, R., Guillemot, F., Serup, P. and